

# Planar Rigid Body Motion Extraction from Motor Vehicle Collision Testing Conducted under United States Safety Testing Protocols

Jai Singh<sup>1</sup>

<sup>1</sup>Biomechanical Engineering Analysis & Research Inc.

2060-D Avenida de los Arboles, No. 487, Thousand Oaks, California 91362, USA

\*\*\*

**Abstract** - In the field of mechanics, displacement is the result of a body undergoing a change in configuration and consists of rigid body modes and deformation. The use of accelerometers, rigidly attached to judiciously determined locations on a body undergoing displacement, coupled with the appropriate equations of mathematical physics, serves as a normative approach, across multiple application areas, for quantifying and qualifying the kinematic response associated with rigid body modes of motion. In this regard, the subject study is bipartite in nature. The first aspect is the development and presentation of the underlying theory. This consists of using a frame referenced approach to derive the salient equations for rigid body accelerometry, for general motion, followed by the reduction to the case of planar motion. The second aspect is the application of this theory to determine the planar kinematic response of production motor vehicles tested for compliance and assessment purposes, under United States safety testing protocols. Using a specific example, it is shown that the planar kinematic responses depends upon the choice of accelerometers comprising the array. Excluding an outlier case, the difference in the reconstructed responses was most apparent in the regards to the translational test vehicle affixed longitudinal axis and corresponding inertial frame axis. The relative differences in the response time histories are evaluated by dynamic time warping analysis and normalized  $L_1$  sequence norm differences. The accelerometer based analysis is supplemented by the use of videogrammetry analysis and a restricted general motion analysis.

**Key Words:** Rigid body dynamics, lateral impact, United States compliance testing

## 1. INTRODUCTION

The use of body-fixed linear accelerometers for elucidating the kinematic response characteristics of a body undergoing prismatic, rotational or general motion is common practice in multiple fields of endeavour. These fields include, but are not limited to, biomechanical engineering [1-7], motor vehicle crashworthiness [8-10] and aerospace engineering [11]. These application archetypes, along with others not specifically listed in the previous statement, are merely contextual and are predicated upon a singular and consistent mathematical framework. The general mathematical framework in

question is that of rigid body dynamics. Contextually, when an event under consideration involves the motion of a body consisting purely of rigid body modes or that which can be modelled, in sufficient part, as representing rigid body motion, the use of peripheral point, body fixed, linear acceleration measurements allows for the elucidation of the motion of the center of mass of the body [12-13].

For a body undergoing rigid body generalized spatial motion (i.e. motion in  $\square^3$ ), there are six degrees of freedom that require determination for fully characterizing the motion. These consist of three prismatic (i.e. translational) degrees of freedom and three rotational degrees of freedom. For the case of planar motion (i.e. motion in  $\square^2$ ) the number of degrees of freedom reduce to three and consist of two prismatic degrees of freedom and one rotational degree of freedom. As a result, the use of a sensor block consisting of three linear accelerometers and three angular rate sensors, arranged in orthogonal configuration, located at the center of mass of a rigid body, is sufficient for fully characterizing the generalized spatial motion of a rigid body. Also, the use of a sensor block consisting of two linear accelerometers and one angular rate sensor with the former arrayed in an in-plane orthogonal configuration and with the latter measuring the rotation rate orthogonal to the plane, positioned at the center of mass of the rigid body, is sufficient for fully characterizing planar rigid body motion.

In practice, however, when only linear accelerometers are employed at peripheral locations, the total number of uniaxial linear accelerometers exceeds the minimum values noted above. Furthermore, measurements from sensors, the total number exceeding the required minimum, allows for redundancy, which in turn leads to an ability for employment of methods such as least squares error estimation. Common configurations for generalized spatial motion include the 3-2-2-2 array consisting of a central triaxial and three biaxial accelerometers [2, 14-16] and the 3-3-3 array consisting of three peripheral triaxial accelerometers [17]. Other arrangements [18] and geometric requirements regarding the accelerometer array configuration for planar motion have also been presented in the literature [19].

The evaluation of collisions that are planar or that can be sufficiently modeled as being planar has been the focus of the motor vehicle accident reconstruction engineering

literature. Cheng and Guenther (1989) used a series of lateral impact collision tests to evaluate the relationship between center of mass translational velocity and the translational velocity at peripheral locations [20]. Bundorf (1996) presented the results of applying planar rigid body dynamics theory to determine the velocity change at the center of mass of a collision partner based upon peripheral accelerometer data [21]. McHenry and McHenry (1997) presented a methodology for employing data from arbitrarily positioned accelerometers within the context of reanalyzing the Research Input for Computer Simulation of Automobile Collisions (RICSAC) collision tests [22]. Marine and Werner (1998) presented the results for determining planar motion starting with a basis of data from two biaxial accelerometers [23]. Finally, Struble et al. (2001), within the context of residual damage based modeling, presented results in regards to the evaluation of collision testing conducted under United States (US) safety testing protocols [24].

In the United States, the National Highway Traffic Safety Administration (NHTSA), under the Department of Transportation (DOT), serves as the principle source for public dissemination of data generated from testing conducted for the following purposes: Federal Motor Vehicle Safety Standard (FMVSS) compliance, New Car Assessment Program (NCAP) testing, testing protocol development and testing conducted for research purposes. Testing conducted for FMVSS compliance or NCAP purposes is done so, in theory, in accordance with standardized protocols and within strict tolerances. Publicly available data, for any given test, includes any or all of the following: the report generated by the testing contractor, high speed video footage, photographic data and raw instrumentation data.

From the practice perspective, the quantification of vehicle platform and impacted region specific structural strength parameters relies on the reduction of controlled collision test data. The publicly available data described in the preceding paragraph is quite befitting of the type of controlled collision test data that is usable for field specific evaluations. The majority of commonly employed methods rely on this data for quantifying mathematical model coefficients that relate either the collision force or the internal work (IW) associated with a collision and the residual damage profile that is generated by a collision. The most common mathematical models rely upon a correlation (presumed or otherwise) between peak collision force, normalized per unit width of direct contact damage) and the depth of residual damage and/or equivalent barrier velocity (EBS), which is defined as the velocity at which a vehicle would have to strike a fixed, rigid, massive barrier (FRMB), such that (a) the initial kinetic energy of the vehicle is absorbed by the vehicle structure and (b) the internal work absorbed (IWA) is fully dissipated, and the depth of residual damage. These methods have been reviewed previously [25]. From a

strict engineering perspective, these methods correlate a readily observable terminus of separation phase parameter (the residual damage depth) to a closure phase parameter (peak collision force or EBS).

For frontal impact collision testing such as that conducted for FMVSS 208D compliance or frontal impact NCAP testing, the collision configuration is collinear and with the second collision partner being a FRMB. During the collision, the FRMB can be treated as non-deflecting (i.e. rigid) and non-displacing (i.e. fixed). As a result, the initial kinetic energy of the test vehicle can be treated as fully absorbed during closure. A portion of this IWA is dissipated and a portion is recovered during the separation phase. The peak longitudinal structural deflection experienced by the test vehicle can readily be determined from the dynamic center of mass deceleration (when a barrier load cell is present) or from test vehicle affixed accelerometers. In such an analysis, one can readily neglect any rigid body motion experienced by the test vehicle.

The relevant side impact testing conducted under NHTSA protocols consists of compliance testing for FMVSS 214D or high-speed lateral NCAP testing. The protocols for both tests involve a moving deformable barrier (MDB) striking the left side of a stationary test vehicle. For both tests, the impact is orthogonal and with the wheels of the MDB rotated 27° from the MDB longitudinal axis (crab angle). A primary salient difference between the protocols for the two tests is that the compliance testing is conducted with the MDB at nominal initial velocity of 52.9 KPH and with the assessment testing conducted with the MDB at nominal initial velocity of 61.9 KPH. Additional details for each test type, including information on the construction and dimensions of the MDB, can be found elsewhere [26-27]. In both of these tests, both the MDB and the test vehicle undergo deformation during the collision and since both collision partners are not fixed, both also undergo gross motion during the collision phase. As a consequence, any collision phase displacement solution based upon the use of collision partner affixed accelerometers requires the removal of the rigid body modes of motion in order to determine the structural deflection.

These introductory paragraphs lead directly to the objectives of the subject work. The first is the establishment of the underlying theory for the use of any sufficient number,  $K_i$ , linear uniaxial accelerometers, being equal to or greater in number than a minimum number (based on configuration and spatial dimension under consideration), associated with the  $i^{\text{th}}$  body undergoing rigid body motion, for determining the center of mass translational kinematic response and for determining the rotational kinematic response of the body. The second objective is the application of this theory for the estimation of collision phase rigid body motion

experienced by test vehicles subjected to FMVSS 214D or high speed lateral NCAP testing.

## 2. Theory

Consider a vector,  $\xi$ , in  $\mathbb{R}^n$ , where  $n \in \mathbb{N}$  denotes the spatial order of Euclidean space under consideration, as expressed in two frames of reference A and C. Furthermore, consider both frames of reference as rectangular Cartesian characterizations of the spatial order of Euclidean space under consideration. Mathematically, the vector  $\xi$  can be alternatively expressed as:

$${}^A\xi = \sum_{p=1}^n {}^A\xi_p \mathbf{e}_{Ap} \quad {}^C\xi = \sum_{p=1}^n {}^C\xi_p \mathbf{e}_{Cp} \quad (1)$$

Where  $\mathbf{e}_{Ap}$  and  $\mathbf{e}_{Cp}$   $\{p: 1 \leq p \leq n\}$  denotes the set of orthonormal unit vectors that are associated with the rectangular characterization of the A and C frame of reference, respectively. The scalar terms  ${}^A\xi_p$  and  ${}^C\xi_p$  denote the component of the vector  $\xi$  projected along the  $p^{\text{th}}$  unit vector of the A and C frame of reference, respectively. When  $\xi$  represents a position vector, the first time derivative of  $\xi$  represents a velocity vector. Taking the first equation under (1) and differentiating with respect to time:

$$\frac{d}{dt} {}^A\xi = {}^A\dot{\xi} = \sum_{p=1}^n \left( \left( \frac{d}{dt} {}^A\xi_p \right) \mathbf{e}_{Ap} + {}^A\xi_p \left( \frac{d}{dt} \mathbf{e}_{Ap} \right) \right) \quad (2)$$

Clearly, as shown by equation (2), the time derivative of the vector  $\xi$  depends upon the frame of reference in which the derivative is being taken. When the derivative is taken with respect to the A frame, the time derivatives of the unit vectors of the A frame are zero valued. This finding is not unique to the A frame in that the frame designation, for this finding, is arbitrary (e.g. the same finding would hold for the C frame expression of  $\xi$ , its first time derivative and the time derivative of the unit vectors of the C frame being zero valued). This leads to the following definition of a simple frame-referenced time derivative.

$$\frac{d}{dt} {}^A\xi = {}^A\dot{\xi} = \sum_{p=1}^n \left( \frac{d}{dt} {}^A\xi_p \mathbf{e}_{Ap} \right) \quad \frac{d}{dt} {}^C\xi = {}^C\dot{\xi} = \sum_{p=1}^n \left( \frac{d}{dt} {}^C\xi_p \mathbf{e}_{Cp} \right) \quad (3)$$

One may also define a mixed derivative in which the expression frame of the vector serving as the operand of the derivative operator differs from the derivative frame [28]. Using the two frames of reference noted above:

$$\begin{aligned} \frac{d}{dt} {}^C\xi &= \frac{d}{dt} {}^A\xi + {}^C\omega_A \times {}^A\xi \\ {}^C\dot{\xi}_A &= {}^A\dot{\xi}_A + {}^C\omega_A \times {}^A\xi \end{aligned} \quad (4)$$

In equation (4), the angular velocity vector  ${}^C\omega_A$  is the angular velocity of the A frame, about the C frame, as expressed in terms of the components of the A frame. Equation (4) is applicable to any vector that is expressed

in one frame and for which the frame-referenced time derivative is taken in another frame. Equation (4) can be rewritten in an equivalent form by replacing the cross product with the vector-matrix product obtained from the skew-symmetric (i.e. antisymmetric) matrix associated with the first vector multiplied by the second vector.

$${}^C\dot{\xi}_A = {}^A\dot{\xi}_A + {}^C\omega_A \times {}^A\xi = {}^A\dot{\xi}_A + {}^C\tilde{\omega}_A {}^A\xi \quad (5)$$

### 2.1 Inertial and body frames of reference

For the subject work, the theoretical development proceeds by deriving the operative equations for three spatial dimensions ( $n = 3$ ) and then employing the appropriate simplifications for planar ( $n = 2$ ) motion. We proceed by defining an inertial frame of reference (the G frame), which for the purpose of the subject work, is taken as a ground fixed frame of reference. This frame is characterized as being rectangular Cartesian with origin  $\mathbf{O}$  and an orthonormal triad of unit vectors  $\mathbf{E}_1$ ,  $\mathbf{E}_2$  and  $\mathbf{E}_3$  (with respective corresponding coordinate axes  $\mathbf{X}$ ,  $\mathbf{Y}$  and  $\mathbf{Z}$ ).

For a system comprised of  $N_B$  discrete bodies, there will be  $N_B$  individual body frames of reference. For the  $i^{\text{th}}$  frame of reference, associated with body  $B_i$ ,  $\{i: 1 \leq i \leq N_B\}$ , the characterization is again one of rectangular Cartesian with origin  $\mathbf{o}_i$  and orthonormal triad of unit vectors  $\mathbf{e}_{i1}$ ,  $\mathbf{e}_{i2}$  and  $\mathbf{e}_{i3}$  (with respective corresponding coordinate axes  $\mathbf{x}_i$ ,  $\mathbf{y}_i$  and  $\mathbf{z}_i$ ). For the  $k^{\text{th}}$  point of interest, the G frame and  $B_i$  frame expressions of the position vector  $\mathbf{r}_k$  can be related by the following:

$${}^G\mathbf{r}_k(t) = {}^G\mathbf{r}_{o_i}(t) + {}^G\mathbf{R}_{B_i}(t) {}^B_i\mathbf{r}_k(t) \quad (6)$$

Where  ${}^G\mathbf{r}_k(t)$  is the G frame expression of the position vector  $\mathbf{r}_k(t)$ ,  ${}^B_i\mathbf{r}_k(t)$  is the  $B_i$  frame expression of the position vector  $\mathbf{r}_k(t)$ ,  ${}^G\mathbf{r}_{o_i}(t)$  is the G frame expression of the origin of coordinates of the  $B_i$  frame and  ${}^G\mathbf{R}_{B_i}(t)$  is the direction cosine matrix that transforms vector components from the  $B_i$  frame to the G frame. The DCM is an orthogonal matrix (i.e.  $\mathbf{R}^T = \mathbf{R}^{-1}$ ). The inverse of the DCM  ${}^G\mathbf{R}_{B_i}(t)$ , denoted as  ${}^B_i\mathbf{R}_G(t)$ , which transforms vectors components from the G frame to the  $B_i$  frame, is obtained by taking the transpose of the former (the transpose and inverse being equal due to the orthogonal property of the matrix). The DCM can be parameterized in a number of ways such as with Euler angles or quaternions. Solely for the sake of simplifying the presentation, the explicit time-dependence shown in equation (6) is generally not shown in the following development. It should be noted, however, that the time-dependence is patent and should not be forgotten. To avoid any confusion over this point, equation (6) is presented again, in equivalent form, as equation (7).

$${}^G \mathbf{r}_k = {}^G \mathbf{r}_{o_i} + {}^G R_{B_i} {}^{B_i} \mathbf{r}_k \quad (7)$$

Algebraic rearrangement of equation (7) leads to the following:

$$\begin{aligned} {}^{B_i} \mathbf{r}_k &= {}^G R_{B_i}^{-1} ({}^G \mathbf{r}_k - {}^G \mathbf{r}_{o_i}) \\ &= {}^G R_{B_i}^T ({}^G \mathbf{r}_k - {}^G \mathbf{r}_{o_i}) = {}^{B_i} R_G ({}^G \mathbf{r}_k - {}^G \mathbf{r}_{o_i}) \end{aligned} \quad (8)$$

There are two additional relationships that are of use in the subsequent theoretical derivation. The first is the relationship between the time derivative of the DCM premultiplied frame-referenced vector and the frame-referenced time derivative. For any two frames A and C:

$$\frac{d}{dt} ({}^C R_A {}^A \mathbf{r}_k) = {}^C R_A \left( \frac{d}{dt} {}^A \mathbf{r}_k \right) \quad (9)$$

The second is the relationship between the G frame and  $B_i$  frame expressions of the antisymmetric angular velocity matrices.

$${}^G \tilde{\omega}_{B_i} = {}^G R_{B_i} {}^{B_i} \tilde{\omega}_{B_i} {}^{B_i} R_G \quad {}^{B_i} \tilde{\omega}_{B_i} = {}^{B_i} R_G {}^G \tilde{\omega}_{B_i} {}^G R_{B_i} \quad (10)$$

## 2.2 Derivative kinematics

Taking the first G derivative of equation (7), making use of equation (4) and equation (9):

$$\begin{aligned} \frac{d}{dt} {}^G \mathbf{r}_k &= \frac{d}{dt} ({}^G \mathbf{r}_{o_i} + {}^G R_{B_i} {}^{B_i} \mathbf{r}_k) \\ &= {}^G \dot{\mathbf{r}}_{o_i} + {}^G R_{B_i} \left( \frac{d}{dt} {}^{B_i} \mathbf{r}_k \right) \\ {}^G \dot{\mathbf{r}}_k &= {}^G \dot{\mathbf{r}}_{o_i} + {}^G R_{B_i} ({}^{B_i} \dot{\mathbf{r}}_k + {}^{B_i} \omega_{B_i} \times {}^{B_i} \mathbf{r}_k) \end{aligned} \quad (11)$$

When the point k is fixed in the  $B_i$  frame, the position vector  $\mathbf{r}_k$  in the  $B_i$  frame, is fixed. As a consequence of this, the  $B_i$  frame-referenced time derivatives of that position vector are zero valued. In such a case, equation (11) reduces to the following:

$$\frac{d}{dt} {}^G \mathbf{r}_k = {}^G \dot{\mathbf{r}}_k = {}^G \dot{\mathbf{r}}_{o_i} + {}^G R_{B_i} ({}^{B_i} \omega_{B_i} \times {}^{B_i} \mathbf{r}_k) \quad (12)$$

Taking the G derivative of equation (12):

$$\begin{aligned} \frac{d}{dt} {}^G \dot{\mathbf{r}}_k &= \frac{d}{dt} {}^G \dot{\mathbf{r}}_{o_i} + {}^G R_{B_i} \left( \frac{d}{dt} ({}^{B_i} \omega_{B_i} \times {}^{B_i} \mathbf{r}_k) \right) \\ &= \frac{d}{dt} {}^G \dot{\mathbf{r}}_{o_i} + {}^G R_{B_i} \left( \left( \frac{d}{dt} {}^{B_i} \omega_{B_i} \right) \times {}^{B_i} \mathbf{r}_k + \right. \\ &\quad \left. {}^{B_i} \omega_{B_i} \times \left( \frac{d}{dt} {}^{B_i} \mathbf{r}_k \right) \right) \end{aligned} \quad (13)$$

The G derivative of the angular velocity of the body frame, about the inertial frame, expressed in the body frame, is obtained by applying equation (4).

$$\begin{aligned} \frac{d}{dt} {}^G {}^{B_i} \omega_{B_i} &= \frac{d}{dt} {}^{B_i} \omega_{B_i} + {}^{B_i} \omega_{B_i} \times {}^{B_i} \omega_{B_i} \\ &= \frac{d}{dt} {}^{B_i} \omega_{B_i} + \mathbf{0} = {}^{B_i} \dot{\omega}_{B_i} = {}^{B_i} \alpha_{B_i} \end{aligned} \quad (14)$$

The G derivative of the  $B_i$  frame expression of  $\mathbf{r}_k$  is given by equation (5), noting that the  $B_i$  frame-referenced time derivative of the  $B_i$  frame expression of  $\mathbf{r}_k$  is zero-valued when k is fixed in the body frame.

$$\begin{aligned} \frac{d}{dt} {}^{B_i} \mathbf{r}_k &= \frac{d}{dt} {}^{B_i} \mathbf{r}_k + {}^{B_i} \omega_{B_i} \times {}^{B_i} \mathbf{r}_k \\ &= \mathbf{0} + {}^{B_i} \omega_{B_i} \times {}^{B_i} \mathbf{r}_k \\ &= {}^{B_i} \omega_{B_i} \times {}^{B_i} \mathbf{r}_k \end{aligned} \quad (15)$$

Substitution of equations (14) and (15) into equation (13) results in the following:

$${}^G \ddot{\mathbf{r}}_k = {}^G \ddot{\mathbf{r}}_{o_i} + {}^G R_{B_i} \left( \begin{aligned} &{}^{B_i} \dot{\omega}_{B_i} \times {}^{B_i} \mathbf{r}_k + \\ &{}^{B_i} \omega_{B_i} \times ({}^{B_i} \omega_{B_i} \times {}^{B_i} \mathbf{r}_k) \end{aligned} \right) \quad (16)$$

The act of premultiplying a vector by a DCM, thereby changing its expression frame, is referred to as applying a kinematic transform. Doing so in regards to equation (16), using the DCM that transforms components from the G frame to the  $B_i$  frame:

$${}^{B_i} \ddot{\mathbf{r}}_k = {}^{B_i} \ddot{\mathbf{r}}_{o_i} + {}^{B_i} \dot{\omega}_{B_i} \times {}^{B_i} \mathbf{r}_k + {}^{B_i} \omega_{B_i} \times ({}^{B_i} \omega_{B_i} \times {}^{B_i} \mathbf{r}_k) \quad (17)$$

The process of arriving at equation (17), from equation (16), employs the orthogonality property of the DCM. The G frame expression of the acceleration at point k can also be written as the vector addition of the acceleration due to gravity, and a second term,  ${}^G \mathbf{f}_k$ , which is referred to as the specific force.

$${}^G \ddot{\mathbf{r}}_k = {}^G \mathbf{f}_k + {}^G \mathbf{g} \quad (18)$$

## 2.3 Body fixed accelerometers

The term sensor block, as used herein, refers to any combination of uniaxial accelerometers that are collocated at a fixed point, k, on body  $B_i$ . The standard combinations consist of a single uniaxial accelerometer, two uniaxial accelerometers (biaxial) or three uniaxial accelerometers (triaxial). For the last two cases, the sensing axes are generally positioned in a mutually orthogonal manner. When the sensing axis of any given uniaxial accelerometer or for any given block is not initially aligned with the relevant principle axes of the underlying body  $B_i$ , a DCM is required for each instrumentation frame to transform the measured acceleration components into components along the relevant principle body frame axes. For the

subject work, as detailed in the next section, the relevant subset of sensor blocks start with the sensing axes aligned along the relevant collision partner principle axes and remain aligned during the course of the collision event. This precludes the necessity of transforming measured accelerations for each block from the block's instrumentation frame into components along the body frame axes.

We define a 3x1 column vector, for each point k, for each body  $B_i$ , at which a sensor block is attached. This vector defines the operative sensing axis under consideration (the operative axis results in unity value for the corresponding vector element with the other two vector elements being zero valued).

$${}^{B_i} \mathbf{s}_k = [s_{ik1} \quad s_{ik2} \quad s_{ik3}]^T \quad (19)$$

As a result, the vectors  $[1 \ 0 \ 0]^T$ ,  $[0 \ 1 \ 0]^T$  and  $[0 \ 0 \ 1]^T$  apply for all cases when an accelerometer axis is aligned along the  $x_i$ -axis,  $y_i$ -axis or  $z_i$ -axis, respectively. The measurements obtained from the accelerometer at point k can therefore be expressed as:

$${}^{B_i} \ddot{\mathbf{r}}_k = ({}^{B_i} \mathbf{s}_k)^T ({}^{B_i} \mathbf{f}_k) = ({}^{B_i} \mathbf{s}_k)^T {}^{B_i} \mathbf{R}_G {}^G \mathbf{f}_k \quad (20)$$

Substitution for the inertial frame expression of the specific force, from equation (18), into equation (20), results in the following:

$${}^{B_i} \ddot{\mathbf{r}}_k = ({}^{B_i} \mathbf{s}_k)^T {}^{B_i} \mathbf{R}_G ({}^G \ddot{\mathbf{r}}_k - {}^G \mathbf{g}) \quad (21)$$

Substitution for the inertial frame expression of the acceleration at point k, from equation (16), into equation (21), followed by expansion and simplification:

$${}^{B_i} \ddot{\mathbf{r}}_k = ({}^{B_i} \mathbf{s}_k)^T {}^{B_i} \mathbf{R}_G \left( {}^G \ddot{\mathbf{r}}_{o_i} + {}^G \mathbf{R}_{B_i} \left( \begin{matrix} {}^{B_i} \dot{\boldsymbol{\omega}}_{B_i} \times {}^{B_i} \mathbf{r}_k + \\ {}^{B_i} \boldsymbol{\omega}_{B_i} \times ({}^{B_i} \boldsymbol{\omega}_{B_i} \times {}^{B_i} \mathbf{r}_k) \end{matrix} \right) - {}^G \mathbf{g} \right) \quad (22)$$

Rearranging this result:

$${}^{B_i} \ddot{\mathbf{r}}_k = ({}^{B_i} \mathbf{s}_k)^T {}^{B_i} \mathbf{R}_G ({}^G \ddot{\mathbf{r}}_{o_i} - {}^G \mathbf{g}) + ({}^{B_i} \mathbf{s}_k)^T ({}^{B_i} \dot{\boldsymbol{\omega}}_{B_i} \times {}^{B_i} \mathbf{r}_k) + ({}^{B_i} \mathbf{s}_k)^T ({}^{B_i} \boldsymbol{\omega}_{B_i} \times ({}^{B_i} \boldsymbol{\omega}_{B_i} \times {}^{B_i} \mathbf{r}_k)) \quad (23)$$

The parenthetical in the first term to the right of the equality in equation (23) is the G frame expression of the specific force at the origin of coordinates of the  $B_i$  frame. When premultiplied by the DCM that transforms components from the G frame to the  $B_i$  frame, it becomes the  $B_i$  frame expression of the specific force at the origin of coordinates of the  $B_i$  frame.

$${}^G \mathbf{f}_{o_i} = {}^G \ddot{\mathbf{r}}_{o_i} - {}^G \mathbf{g} \rightarrow {}^{B_i} \mathbf{R}_G {}^G \mathbf{f}_{o_i} = {}^{B_i} \mathbf{f}_{o_i} \quad (24)$$

Substitution of equation (24) into equation (23):

$${}^{B_i} \ddot{\mathbf{r}}_k = ({}^{B_i} \mathbf{s}_k)^T {}^{B_i} \mathbf{f}_{o_i} + ({}^{B_i} \mathbf{s}_k)^T ({}^{B_i} \dot{\boldsymbol{\omega}}_{B_i} \times {}^{B_i} \mathbf{r}_k) + ({}^{B_i} \mathbf{s}_k)^T ({}^{B_i} \boldsymbol{\omega}_{B_i} \times ({}^{B_i} \boldsymbol{\omega}_{B_i} \times {}^{B_i} \mathbf{r}_k)) \quad (25)$$

The cross product operations in equation (25) can be rewritten as vector-matrix products by employing the antisymmetric matrix forms of the angular acceleration and angular velocity vectors.

$${}^{B_i} \ddot{\mathbf{r}}_k = ({}^{B_i} \mathbf{s}_k)^T {}^{B_i} \mathbf{f}_{o_i} + ({}^{B_i} \mathbf{s}_k)^T ({}^{B_i} \tilde{\boldsymbol{\omega}}_{B_i} {}^{B_i} \mathbf{r}_k) + ({}^{B_i} \mathbf{s}_k)^T ({}^{B_i} \tilde{\boldsymbol{\omega}}_{B_i})^2 {}^{B_i} \mathbf{r}_k \quad (26)$$

The antisymmetric matrix associated with the angular acceleration vector is:

$${}^{B_i} \tilde{\boldsymbol{\omega}}_{B_i} = \begin{bmatrix} 0 & -{}^{B_i} \dot{\omega}_{B_i,3} & +{}^{B_i} \dot{\omega}_{B_i,2} \\ +{}^{B_i} \dot{\omega}_{B_i,3} & 0 & -{}^{B_i} \dot{\omega}_{B_i,1} \\ -{}^{B_i} \dot{\omega}_{B_i,2} & +{}^{B_i} \dot{\omega}_{B_i,1} & 0 \end{bmatrix} \quad (27)$$

The components of the angular velocity vector appear as quadratic products in the square of the skew symmetric matrix associated with the angular velocity vector. The element in row r column s of this matrix is given by the following:

$$\left[ ({}^{B_i} \tilde{\boldsymbol{\omega}}_{B_i})^2 \right]_{rs} = \begin{cases} -\sum_{a=1, a \neq r}^3 ({}^{B_i} \tilde{\boldsymbol{\omega}}_{B_i, a})^2 & \text{for } r = s \\ +{}^{B_i} \tilde{\boldsymbol{\omega}}_{B_i, r} {}^{B_i} \tilde{\boldsymbol{\omega}}_{B_i, s} & \text{for } r \neq s \end{cases} \quad (28)$$

## 2.4 Solution based on the configuration matrix

Following the work of Park and Hong (2011), equation (26) can be rewritten in the following manner [29]:

$${}^{B_i} \ddot{\mathbf{r}}_k = {}^{B_i} \mathbf{J}_k {}^{B_i} \mathbf{y} \quad (29)$$

For each point k, there may be anywhere from one to three acceleration measurements, with each measurement being along one of the sensing axes. This leads to two differing but equivalent methods for formulating the relationship shown by equation (29). The first is by considering all three sensing axes, together, at each point k. Under this approach, for each point k, the left side of the equality in equation (29) becomes a 3 x 1 column vector. Each additional point k extends the column vector by adding three rows. The second approach is to separately consider each sensing axis at each point k. Under this approach, for each sensing axis at each point k, the term on the left side of the equality in equation (29) is the single measured

value of acceleration, along the sensing axis under consideration, at point k. In both cases, the left side of the equality in equation (29) is a  $3k \times 1$  column vector (at each point in time). The body frame expressed term,  $\mathbf{y}$ , is the  $12 \times 1$  column vector of system unknowns. The first three rows of this column vector are:

$${}^{B_i} \mathbf{y}_{k(1-3,1)} = \begin{bmatrix} {}^{B_i} f_{o,1} & {}^{B_i} f_{o,2} & {}^{B_i} f_{o,3} \end{bmatrix}^T \quad (30)$$

Rows four through six of this column vector are:

$${}^{B_i} \mathbf{y}_{k(4-6,1)} = \begin{bmatrix} {}^{B_i} \dot{\omega}_{B_i,1} & {}^{B_i} \dot{\omega}_{B_i,2} & {}^{B_i} \dot{\omega}_{B_i,3} \end{bmatrix}^T \quad (31)$$

Rows seven through nine of this column vector are:

$${}^{B_i} \mathbf{y}_{k(7-9,1)} = \begin{bmatrix} {}^{B_i} \omega_{B_i,1}^2 & {}^{B_i} \omega_{B_i,2}^2 & {}^{B_i} \omega_{B_i,3}^2 \end{bmatrix}^T \quad (32)$$

The final three rows of this column vector are:

$${}^{B_i} \mathbf{y}_{k(10-12,1)} = \begin{bmatrix} {}^{B_i} \omega_{B_i,1} & {}^{B_i} \omega_{B_i,2} & {}^{B_i} \omega_{B_i,3} & {}^{B_i} \omega_{B_i,1} & {}^{B_i} \omega_{B_i,2} & {}^{B_i} \omega_{B_i,3} & {}^{B_i} \omega_{B_i,1} & {}^{B_i} \omega_{B_i,2} & {}^{B_i} \omega_{B_i,3} \end{bmatrix}^T \quad (33)$$

Following the second approach defined above for populating the term  $\mathbf{J}$ , for each sensing axis and each point k, the entry is a  $1 \times 12$  row vector. Columns one through three are:

$${}^{B_i} \mathbf{J}_{k(1,1-3)} = \begin{bmatrix} {}^{B_i} s_{k1} & {}^{B_i} s_{k2} & {}^{B_i} s_{k3} \end{bmatrix} \quad (34)$$

Columns four through six are:

$${}^{B_i} \mathbf{J}_{k(1,4-6)} = \begin{bmatrix} +{}^{B_i} s_{k3} & {}^{B_i} r_{k2} & -{}^{B_i} s_{k3} & {}^{B_i} r_{k1} & +{}^{B_i} s_{k2} & {}^{B_i} r_{k1} \\ -{}^{B_i} s_{k2} & {}^{B_i} r_{k3} & +{}^{B_i} s_{k1} & {}^{B_i} r_{k3} & -{}^{B_i} s_{k1} & {}^{B_i} r_{k2} \end{bmatrix} \quad (35)$$

Columns seven through nine are:

$${}^{B_i} \mathbf{J}_{k(1,7-9)} = \begin{bmatrix} -{}^{B_i} s_{k3} & {}^{B_i} r_{k3} & -{}^{B_i} s_{k3} & {}^{B_i} r_{k3} & -{}^{B_i} s_{k1} & {}^{B_i} r_{k1} \\ -{}^{B_i} s_{k2} & {}^{B_i} r_{k2} & -{}^{B_i} s_{k1} & {}^{B_i} r_{k1} & -{}^{B_i} s_{k2} & {}^{B_i} r_{k2} \end{bmatrix} \quad (36)$$

The final three columns are:

$${}^{B_i} \mathbf{J}_{k(1,10-12)} = \begin{bmatrix} +{}^{B_i} s_{k1} & {}^{B_i} r_{k2} & +{}^{B_i} s_{k3} & {}^{B_i} r_{k1} & +{}^{B_i} s_{k3} & {}^{B_i} r_{k2} \\ +{}^{B_i} s_{k2} & {}^{B_i} r_{k1} & +{}^{B_i} s_{k1} & {}^{B_i} r_{k3} & +{}^{B_i} s_{k2} & {}^{B_i} r_{k3} \end{bmatrix} \quad (37)$$

After final assembly over all sensor axes and points, equation (29) becomes:

$${}^{B_i} \ddot{\mathbf{r}} = {}^{B_i} \mathbf{J} {}^{B_i} \mathbf{y} \quad (38)$$

The column vector to the left of the equality is of the order  $3k \times 1$ . The matrix  ${}^{B_i} \mathbf{J}$ , referred to as the configuration matrix, is of order  $3k \times 12$ . The column vector of system unknowns is of order  $12 \times 1$ . It should be clear that in accordance with this formulation that a minimum of 12 uniaxial acceleration measurements are required (e.g. four triaxial accelerometer blocks). When the number of uniaxial acceleration measurements is exactly 12, the configuration matrix is a square matrix and when non-singular, is invertible. Generally, when the number of

uniaxial acceleration measurements is equal to or exceeds 12, we may define the left matrix inverse of the configuration matrix as:

$${}^{B_i} \mathbf{J}^+ = \left( {}^{B_i} \mathbf{J}^T {}^{B_i} \mathbf{J} \right)^{-1} \left( {}^{B_i} \mathbf{J} \right)^T \quad (39)$$

When the left matrix inverse as defined by equation (39) exists, equation (38) can be inverted.

$${}^{B_i} \mathbf{y} = {}^{B_i} \mathbf{J}^+ {}^{B_i} \ddot{\mathbf{r}} \quad (40)$$

For the special case when the acceleration is measured at the origin of coordinates of the  $B_i$  frame and there are nine uniaxial peripheral acceleration measurements, equation (26) becomes:

$${}^{B_i} \ddot{\mathbf{r}}_k - \left( {}^{B_i} \mathbf{s}_k \right)^T {}^{B_i} \mathbf{f}_{o_i} = \left( {}^{B_i} \mathbf{s}_k \right)^T \left( {}^{B_i} \tilde{\omega}_{B_i} {}^{B_i} \mathbf{r}_k \right) + \left( {}^{B_i} \mathbf{s}_k \right)^T \left( {}^{B_i} \tilde{\omega}_{B_i} \right)^2 {}^{B_i} \mathbf{r}_k \quad (41)$$

The computation of the specific force at the origin of coordinates of the  $B_i$  frame, at time t, requires knowledge of the DCM from the G frame to the  $B_i$  frame, at the same point in time. This DCM, however, is generally unknown at the time of evaluation of equation (41). Leaving the acceleration due to gravity within the measured acceleration at the origin of coordinates of the  $B_i$  frame, allows for the following approximation:

$${}^{B_i} \ddot{\mathbf{r}}_k - \left( {}^{B_i} \mathbf{s}_k \right)^T {}^{B_i} \mathbf{r}_{o_i} \approx \left( {}^{B_i} \mathbf{s}_k \right)^T \left( {}^{B_i} \tilde{\omega}_{B_i} {}^{B_i} \mathbf{r}_k \right) + \left( {}^{B_i} \mathbf{s}_k \right)^T \left( {}^{B_i} \tilde{\omega}_{B_i} \right)^2 {}^{B_i} \mathbf{r}_k \quad (42)$$

The body frame expressed column vector of system unknowns,  $\mathbf{y}$ , reduces to  $9 \times 1$  by removing the first three rows. The individual rows of the configuration matrix reduce to order  $1 \times 9$  with removal of the first three columns.

## 2.5 Planar reduction

The reduction to the planar case greatly simplifies the formulation. In such a reduction, translational motion is constrained to occurring within the plane formed by any two of the three axes of the G frame and with rotational motion occurring about the third orthonormal axis of the G frame. Each body frame is oriented such that one of the three orthonormal axes is coincident with the third orthonormal axis of the G frame. For example, if the plane of analysis is formed by the X and Y axes of the G frame, G frame expressed translational motion has components along those two axes and rotational motion is about the Z axis. If the  $i^{\text{th}}$  body frame is taken such that the  $x_i$  and  $y_i$  axes are the body frame axes within the XY plane, the  $z_i$  axis is coincident with the Z axis. The first resultant simplification is that position, velocity and acceleration vectors for the G frame and each  $B_i$  frame have component  $0\mathbf{e}_{i3} \forall i, t$ . The second simplification is that the DCM between the G frame and the  $i^{\text{th}}$  B frame reduces to a

function of a single rotation angle. This angle is the angle between the +X axis and the +x<sub>i</sub> axis and denoted as θ<sub>i</sub>(t).

$${}^{B_i}R_G(t) = \begin{bmatrix} +\cos(\theta_i(t)) & +\sin(\theta_i(t)) & 0 \\ -\sin(\theta_i(t)) & +\cos(\theta_i(t)) & 0 \\ 0 & 0 & 1 \end{bmatrix} \quad (43)$$

$${}^G R_{B_i}(t) = \begin{bmatrix} +\cos(\theta_i(t)) & -\sin(\theta_i(t)) & 0 \\ +\sin(\theta_i(t)) & +\cos(\theta_i(t)) & 0 \\ 0 & 0 & 1 \end{bmatrix} \quad (44)$$

For the planar case, we may simply drop the E<sub>3</sub> and e<sub>i3</sub> terms of each translational position, velocity and acceleration vector as they are zero valued. Similarly, the DCMs shown in the previous two equations can be rewritten as 2 x 2 matrices by dropping the third row and third column from each matrix. In regards to equation (29), the body frame expression of the system unknowns reduces to a 4 x 1 column vector and each row of the configuration matrix reduces to a 1 x 4 row vector.

$${}^{B_i}y_k = [{}^{B_i}\ddot{r}_{o,1} \quad {}^{B_i}\ddot{r}_{o,2} \quad {}^{B_i}\dot{\omega}_{B,3} \quad {}^{B_i}\omega_{B,3}^2]^T \quad (45)$$

$${}^{B_i}J_k = \begin{bmatrix} {}^{B_i}s_{k1} & {}^{B_i}s_{k2} & -{}^{B_i}r_{k2} & {}^{B_i}s_{k1} & -{}^{B_i}r_{k1} & {}^{B_i}s_{k1} \\ {}^{B_i}s_{k1} & {}^{B_i}s_{k2} & +{}^{B_i}r_{k1} & {}^{B_i}s_{k2} & +{}^{B_i}r_{k2} & {}^{B_i}s_{k2} \end{bmatrix} \quad (46)$$

In equation (45), the components of the specific force at the B<sub>i</sub> frame origin of coordinates has been replaced by the body frame accelerations at the same point. This is apt for the planar case when gravity is along the E<sub>3</sub> axis and the E<sub>3</sub> and e<sub>i3</sub> axis are coincident. After assembly, the column vector of measured accelerations is of order 2k x 1 and the configuration matrix is of order 2k x 4. When the body frame origin of coordinates acceleration is known, a minimum of biaxial acceleration at one peripheral point or uniaxial acceleration at two peripheral points is needed and with the system unknowns reducing to the angular acceleration and square of the angular velocity. The vector matrix equation becomes:

$$\begin{bmatrix} {}^{B_i}\ddot{r}_{j1} - {}^{B_i}\ddot{r}_{o1} \\ {}^{B_i}\ddot{r}_{j2} - {}^{B_i}\ddot{r}_{o2} \end{bmatrix} = \begin{bmatrix} -{}^{B_i}r_{j2} & -{}^{B_i}r_{j1} \\ +{}^{B_i}r_{j1} & -{}^{B_i}r_{j2} \end{bmatrix} \begin{bmatrix} {}^{B_i}\dot{\omega}_{B,3} \\ {}^{B_i}\omega_{B,3}^2 \end{bmatrix} \quad (47)$$

## 2.6 Numerical integration

The solution to equation (40) yields the time history for the three components of the specific force at the origin of coordinates of the body frame, expressed in the body frame, the components of the angular acceleration of body frame, about the G frame, expressed in the body frame and the algebraic solutions for the squared components of the angular velocity of the body frame, about the G frame, expressed in the body frame. Each component of the angular acceleration can be numerically integrated to

calculate the corresponding angular velocity and angular position. The solution procedure for integrating each angular acceleration is the same and we may express each function as the second derivative of x(t) where x is the component of angular position. The choice of method for numerical integration is not fixed. For the subject work, an explicit method, direct time integration using the central difference method is employed.

As discussed in the following the section, the underlying instrumentation data is discrete data with equal spacing between all data points. The time interval between any two successive points is defined as:

$$h = t_{b+1} - t_b = \Delta t \quad \forall b \quad (48)$$

The Taylor series expansion of x(t) at t = t<sub>b</sub> is:

$$x(t) = \sum_{n=0}^{\infty} \left( \frac{(t-t_b)^n}{n!} \left( \frac{\partial^n x}{\partial t^n} \right)_b \right) \quad (49)$$

In equation (49), the subscript of b on the n<sup>th</sup> partial derivative of x with respect to t refers to evaluation at t = t<sub>b</sub>. Writing equation (49) at time step b+1:

$$x_{b+1} = x_b + h \left( \frac{\partial x}{\partial t} \right)_b + \frac{h^2}{2} \left( \frac{\partial^2 x}{\partial t^2} \right)_b + \frac{h^3}{6} \left( \frac{\partial^3 x}{\partial t^3} \right)_b + \dots \quad (50)$$

Writing equation (49) at time step b-1:

$$x_{b-1} = x_b - h \left( \frac{\partial x}{\partial t} \right)_b + \frac{h^2}{2} \left( \frac{\partial^2 x}{\partial t^2} \right)_b - \frac{h^3}{6} \left( \frac{\partial^3 x}{\partial t^3} \right)_b + \dots \quad (51)$$

Taking the first two terms on the right of each equality in the two previous equations and subtracting the second from the first:

$$\left( \frac{\partial x}{\partial t} \right)_b = \dot{x}_b = \frac{1}{2h} (x_{b+1} - x_{b-1}) \quad (52)$$

Taking the first three terms from the right of each equality in equations (50) and (51) followed by addition of the results:

$$\left( \frac{\partial^2 x}{\partial t^2} \right)_b = \ddot{x}_b = \frac{1}{h^2} (x_{b-1} - 2x_b + x_{b+1}) \quad (53)$$

For the subject problem, the angular velocity and angular position are known at the initial point in time. Also, from the solution to equation (40), the angular acceleration is known. The first step to the integration of the angular acceleration requires the calculation of the angular position at discrete time with index b = -1. To obtain this value, equation (52) is first solved for x<sub>b+1</sub> and the result is substituted into equation (53). Rearranging the result leads to the following:

$$x_{b-1} = x_b - h\dot{x}_b + \frac{1}{2}h^2\ddot{x}_b \quad (54)$$

Setting  $b = 0$  in equation (54) allows for the solution for  $x_1$ . Once this value is known, the solutions for the displacement  $x_{b+1}$  is solved from equation (53) followed by the velocity at index  $b$  from equation (52). Once the angular position is known for each time step, the DCM from the body frame to the G frame at each time step can be determined followed by transforming the body frame expressed specific force at the origin of coordinates to the G frame. The G frame expression of the acceleration of the center of coordinates of the body frame can then be obtained from the first equation under (24). The result for each axis along the G frame axes can then be numerically integrated to calculate the G frame velocity and displacement/position time histories.

### 3. MATERIALS AND METHODS

The NHTSA Vehicle Crash Test Database (VCTB) was queried for FMVSS 214D or high-speed lateral NCAP testing and test number v007153, the high-speed lateral NCAP test for a 2011 Nissan Altima 2.5S four door sedan, was randomly selected [30]. The contractor report, videos and instrumentation data (in ASCII format) were downloaded directly from the NHTSA website. Before proceeding with a discussion of the data reduction, it is first important to consider some of the commonalities of the procedures for these kinds of tests. Shown in Figure 1 is a schematic depicting a plan view of the collision partners at the start of the closure phase.

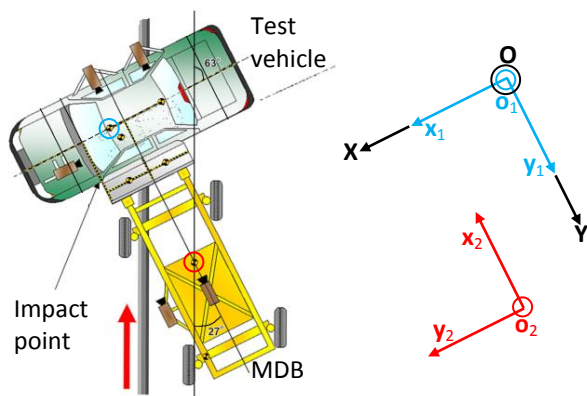


**Fig -1:** Schematic of the configuration of the collision partners at the start of the closure phase (in plan view).

The light blue circle in the image on the left shows the location of the origin of coordinates of the test vehicle. This circle ( $O_1$ ) is shown on the drawing to the right along with the coordinate axes for the test vehicle. The same applies for the red circle ( $O_2$ ) in regards to the origin of coordinates of the MDB. The G frame origin of coordinates ( $O$ ) and axes are shown as being coincident with the test vehicle origin and axes at the start of closure.

The sign convention shown in the Figure follows ISO 15037-1 with the  $x_i$ -axis along the longitudinal centerline of the collision partner in reference (here synonymous

with undeformed) condition (+ directed from aft to fore). The  $y_i$ -axis is oriented along the lateral axis of the collision partner in reference condition (+ directed from right to left). The  $z_i$ -axis is oriented vertically (+ from base to top). The body frame coordinate axes, therefore, form a right handed coordinate system. The configuration of the G frame coordinate axes are chosen to match the configuration of the body frame coordinate axes. In this regard, the  $Z$  axis is positive from ground, upwards, and therefore the acceleration due to the gravity of the Earth is negatively signed. The origin of the G frame ( $O$ ) can be placed arbitrarily but as shown, is coincident with the origin of coordinates of the test vehicle frame ( $O_1$ ) at the start of the closure phase. For both the test vehicle and the MDB, the origin of coordinates (i.e. the respective B frame origin of coordinates) for each is located at the static center of mass for each. In the case of pure rigid body motion, each body frame would therefore be a central frame. Finally, for the subject planar case, counterclockwise rotations are positively signed.

The standard followed by NHTSA is not the ISO standard and instead is the vehicle dynamics standard used by the Society of Automotive Engineers (SAE). The SAE J670 standard follows a sign convention that is a  $180^\circ$  rotation about the  $x_i$ -axis. On a prima facie basis, this requires multiplying all reported translational quantities and dimensions along the  $y_i$  and  $z_i$  axes by minus one in order to convert values to be in accordance with the ISO standard.

The accelerometer block placement for each collision partner, the number of sensing axes per block and the orientation of each sensing axis for these tests is standardized. For the MDB, there are two blocks. One is a triaxial block located at the static center of mass and oriented along the reference axes of the MDB. The second is a biaxial block placed at the junction of the left longitudinal rail and the lateral crossmember that is in-line with the rear wheels. The sensing axes for this biaxial block are along the  $x_2$  and  $y_2$  axes. For the test vehicle, the standard configuration is of 13 discrete sensor block locations. These are listed in Table 1.

**Table -1:** Test vehicle sensor block configuration. The terms right (R) and left (L) are from the perspective of the test vehicle.

Location	Description	$x_1$	$y_1$	$z_i$
1	R sill @ front seat	X	X	X
2	R sill @ rear seat	X	X	X
3	Rear floorpan above axle	X	X	X
4	L sill @ rear door		X	
5	L sill @ front door		X	
6	R rear occupant compartment		X	
7	L B-pillar lower		X	
8	L B-pillar mid		X	
9	L A-pillar lower		X	

10	L A-pillar mid		X	
11	L front seat track		X	
12	L rear seat structure		X	
13	Vehicle center of mass	X	X	X

In certain cases there is a biaxial (for the  $x_1$  and  $y_1$  directions) accelerometer attached to the top of the engine. From the general perspective, accelerometers at locations 1, 2, 3, 6, 12 and 13 would be expected to be in areas that experience the least deformation and therefore are most apt for use in determining the rigid body motion of the test vehicle. The coordinate locations for each block are provided in the contractor report for each test. The values are reported with respect to a set of reference planes (e.g. rear surface of vehicle, vehicle centerline and ground plane) and can readily be converted to the subject body frame by first multiplying all  $y$  and  $z$  coordinate values by minus one and then subtracting the reported center of mass location from all values. The same approach is used for the reported MDB sensor block locations.

The initial velocity for the test vehicle in all cases of this type is known as being zero valued. Because of the crab angle of the MDB, the initial velocity is not purely along the  $x_2$  axis. Instead, the components of the initial MDB velocity along the MDB axes are  $\{v_{MDB0} \cos(-27^\circ), v_{MDB0} \sin(-27^\circ)\}$ .

Returning to the data evaluation, a custom-written software program using a symbolic mathematics package (Mathematica v.10.2; Wolfram Research Inc., Champaign, Illinois, USA) was created for conducting all of the necessary evaluations. The imported instrumentation data, in zip format, was unzipped and the resulting files were queried for the NHTSA Entrée V5 file. This file, generally, consists of a database entry of relevant data, for each test, in standardized format. This file was imported and the instrumentation section was segmented from the EV5 file using known boundary text delimiters. This was followed by using a text string search, using the known four letter abbreviations for each sensor block location, to extract each line associated with each test vehicle and MDB affixed accelerometer block. This data was further segmented by instrumentation channel, with each channel being uniaxial in nature. Each line of data from the resultant contained a unique signal number, corresponding to the extension of the ASCII file name in the unzipped file folder. This approach ensured that the correct data file was imported for each sensing axis of each sensor block for both the test vehicle and the MDB.

The imported, single channel accelerometer data, for each file, consisted of a sequence of pairwise points in {time, value} format. This data was raw, unfiltered, discrete data. For each channel for which data was reported, there was 30 milliseconds of pre-impact data. The start of the impact (i.e. the start of the closure phase) was verified by

(a) examination of the high speed video files and (b) examination of the front face of the MDB affixed tapeswitch data. For all channels, the sampling rate was 10 kHz and with a resulting time step of 0.1 milliseconds. The filtering requirement for accelerometer data is by means of SAE channel frequency class (CFC) 60 filtering. This is a digital, four pole, Butterworth low pass filter with linear phase (obtained by passing the data through the filter twice, once forward and once backward) and with the following characteristics: 100 Hz 3 dB cut-off frequency and -30 dB stopband attenuation.

This filter was implemented within the symbolic mathematics package and with the inclusion of zero valued left and right padding. The validity of the subject implementation of the CFC filter was checked by comparing the results of filtering against those generated using an alternative software package that has a native inception of the filter (DPlot v.2.3.5.7; HydeSoft Computing, LLC, Vicksburg, Mississippi, USA) along with comparison of the results generated using NHTSA's PlotBrowser utility [31]. The custom written code allowed for batch processing of all accelerometer data. In the experience of the author, the CFC filter has difficulties with removing low frequency noise whose signal power is within the regime of the frequency response of the desired signal data. Furthermore, the filter generates artifacts when there are substantive slope changes in the underlying data. However, there is no general method for correcting these issue and the development of an alternative filtering methodology was beyond the scope of the subject work. The sign of the filtered data for the  $y_i$  and  $z_i$  data was changed and the signals were truncated to start at time  $t_0 = 0$ . The signal values at  $t_0$ , for each signal, were subtracted from all data points for each signal.

The following evaluations were undertaken using the appropriate set of equations described in the previous section: (a) determination of the angular kinematics and inertial frame position and velocity time-histories using the static center of mass accelerometer and one peripheral biaxial accelerometer; (b) determination of the angular kinematics and reconstruction of the center of mass inertial frame kinematic responses using all peripheral biaxial accelerometer combinations; (c) determination of the angular kinematics and reconstruction of the center of mass inertial frame kinematic responses using a subset of accelerometers located outside of the direct impact area. The work of Sarin et al. (2010) served as guide for establishing methods for comparing the time series generated for each kinematic parameter for each evaluation [32].

The warping distance function, a native function within the Mathematica framework, was used for this purpose. The warping distance is defined as the minimum distance for correspondence between a reference sequence and a query sequence. Mathematically, it is defined as:

$$\sum_{i=1}^k d(s_1 n_i, s_2 m_i) \tag{55}$$

Where  $s_1 n_i$  and  $s_2 m_i$  are corresponding elements in the reference sequence and query sequence, respectively. The function  $d()$  is the distance function that is employed. In the subject case, the Euclidean distance was used. The magnitude difference was determined from the dynamically time warped (DTW) modified signals, using the  $L_1$  norm, as:

$$\frac{\|a - b\|_1}{\|b\|_1} \tag{56}$$

Equation (56) produces two, generally differing, solutions depending on the time series used for normalization. For any  $P$  configurations, there will be  $P^2$  potential options, which can be expressed as a  $P \times P$  square matrix. The diagonal of the matrix is a diagonal consisting of zero-valued elements.

An alternative method was devised to assess the angular kinematics (given the lack of angular rate sensor data). This approach fits within the broad category of videogrammetry. A geometrically correct reference vehicle model, in Wavefront OBJ format was obtained by the author (<https://www.3dcadbrowser.com/>). The vehicle model was correctly scaled using an open source 3D modeling and animation package (Blender v.2.83.1; Blender Foundation; <https://www.blender.org/>). A commercially available videogrammetry software package (SynthEyes, 1905, 2004 Build 1047; Andersson Technologies LLC, Adairsville, Georgia, USA) was used to evaluate the planar angular kinematics. In this regard, the wide view high speed film footage (video 2) was imported into the software package. The lack of a priori knowledge of the scale of the scene, for the field of view of the camera, proved to be problematic when it came to solving for the camera parameters. Instead, a number of test vehicle fixed points, in regions of the vehicle that were deemed to have minimal deformation, were tracked through all frames of the video footage. The scaled 3D vehicle model was then imported as a mesh, onto a moving object construct within the software. The mesh was attached to the moving object by linking the test vehicle fixed trackers to their corresponding physical points on the mesh model. This approach allowed for the motion of the test vehicle to be determined, using the scale implicit within the model.

The final evaluation was the evaluation using the general motion formulation. Equation (42) was used to determine the body frame expressions of the angular acceleration of the body frame about the inertial frame of reference and the quadratic angular velocity terms involving the body frame expressions of the body frame about the inertial frame. The resultant angular accelerations were integrated to determine the DCM for each of the three elementary rotations. With the composite DCM known,

the antisymmetric form of the body frame expressed angular acceleration of the body frame about the inertial frame of reference was used in conjunction with equation (10) to determine the angular acceleration of the body frame, about the inertial frame of reference, expressed in terms of the inertial frame. Each axis was numerically integrated to determine the corresponding angular velocity and displacement.

#### 4. RESULTS

The filtered truncated test vehicle fixed x-axis accelerometer time histories are shown in Figure 2.

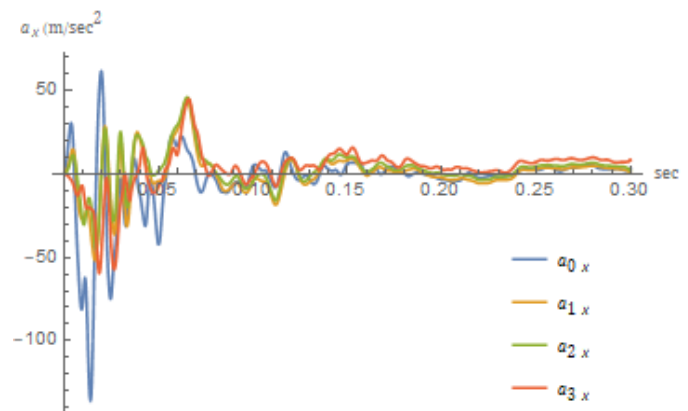


**Fig -2:** Filtered truncated test vehicle fixed x-axis accelerometer time histories. In the legend, the signal referenced as  $a_{0x}$  refers to the static center of mass recorded data. The number in the subscript for the other signals correspond to the locations with the same number as per Table 1.

Acceleration data from 10 of the 13 sensor blocks with a sensing axis aligned along the y-axis of the test vehicle was available. There was no data recorded from the left lower A-pillar sensor (sensor location 9; the commentary for this sensor, in the EV5 file, misidentifies this sensor as being located on the right side of the test vehicle; the misidentification is clear given the y-axis location of the sensor as per the contractor's report) and the left seat track sensor (sensor location 11) due to channel failure. There was no data from sensor location 12 due to the fact that the sensor was not installed. The filtered truncated test vehicle fixed y-axis accelerometers for those accelerometers not on the left side of the test vehicle are shown in Figure 3 and the data from the accelerometers on the left side is shown in Figure 4.

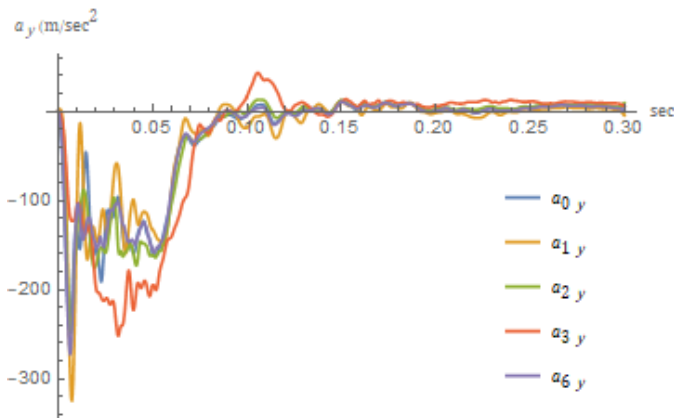


**Fig -3:** Filtered truncated test vehicle fixed  $y$ -axis accelerometer time histories from accelerometers not on the left side of the test vehicle. In the legend, the signal referenced as  $a_{0y}$  refers to the static center of mass recorded data. The number in the subscript for the other signals correspond to the locations with the same number as per Table 1.

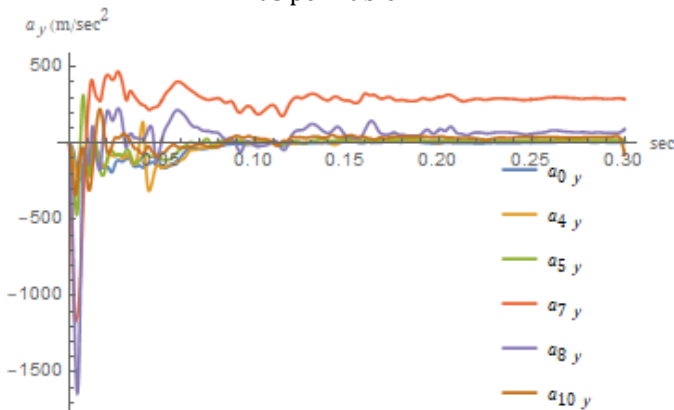


**Fig -4:** Filtered truncated test vehicle fixed  $y$ -axis accelerometer time histories from accelerometers on the left side of the test vehicle. In the legend, the signal referenced as  $a_{0y}$  refers to the static center of mass recorded data. The number in the subscript for the other signals correspond to the locations with the same number as per Table 1.

In the following sections, detailing the results of the accelerometer based angular and translational kinematics, a consistent numbering system is employed to simplify the presentation of the graphical results. The number zero is used as a reference to the static center of mass accelerometer. The numbers one-three refer to solutions based upon the center of mass accelerometer coupled with the corresponding peripheral biaxial accelerometer positioned at locations one-three, as per Table 1. These solutions are based on employing equation (47). The numbers four-seven refer, respectively, to solutions based on using the peripheral accelerometers located at 1-2, 1-3, 2-3 and 1-2-3, as per Table 1.

The most general planar formulation is based upon the use of uniaxial accelerometers (each triaxial sensor block

reducing, for the planar formulation, to a biaxial sensor block consisting of two uniaxial accelerometers). The total number of uniaxial in-plane accelerometers not located at the center of mass and outside of the impact zone is seven (three along the  $x$ -axis of the test vehicle and four along the  $y$ -axis of the test vehicle). With a minimum of four uniaxial in-plane accelerometers required, the total number of options is 64 (the sum of seven choose four through seven choose seven). Four of these cases are the cases referenced as one-four. Space limitations preclude presenting the totality of the other 60. Five additional evaluations were chosen randomly from the set of the other 60 configurations. In sequence, these evaluations are: the use of all seven uniaxial accelerometers (three biaxial plus one uniaxial), using all of the biaxial accelerometers but with the  $y$ -axis accelerometer at location one not used and the single  $y$ -axis uniaxial accelerometer at location six used, using all of the biaxial accelerometers but with the  $y$ -axis accelerometer at location two not used and the single  $y$ -axis uniaxial accelerometer at location six used, using all of the biaxial accelerometers but with the  $y$ -axis accelerometer at location three not used and the single  $y$ -axis uniaxial accelerometer at location six used and finally using all of the biaxial accelerometers but with the  $x$ -axis accelerometer at location one not used and the single  $y$ -axis uniaxial accelerometer at location six used. The numbers eight-12, respectively refer to these configurations.

#### 4.1 Angular kinematics

The calculated angular acceleration response for the test vehicle, as expected, was non-monotonic, and replete with sign reversals and multiple peaks and valleys. The results are shown in Figure 5. The peak values for the angular acceleration are generally within  $\pm 100$  rad/sec<sup>2</sup>, except for case three. The initial angular acceleration is positive for the following cases: 1, 4, 5, 7, 8, 10, 11, 12. All of these cases use the  $y$ -axis accelerometer at location one.

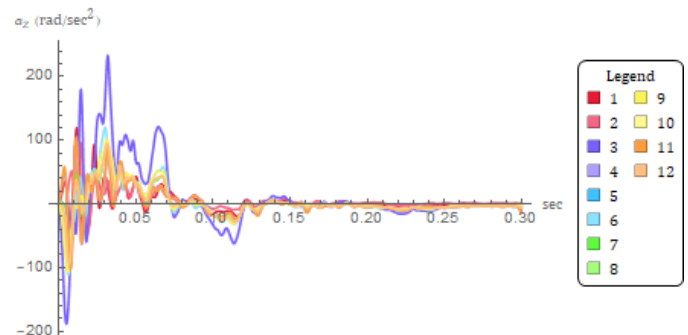


**Fig -5:** Angular acceleration time histories.

The angular velocity response can be categorized as following one of two general descriptions in regards to the initial response from 0 to  $\sim 30$  milliseconds. The first description is of an initial positive valued response

followed by a return towards zero. The second description is of an initial negative response followed by a return towards zero. The cases that fall into the first category are 1, 4, 5, 7, 8, 10, 11 and 12. These are all cases that employ the y-axis accelerometer at location one. The results are shown in Figure 6.

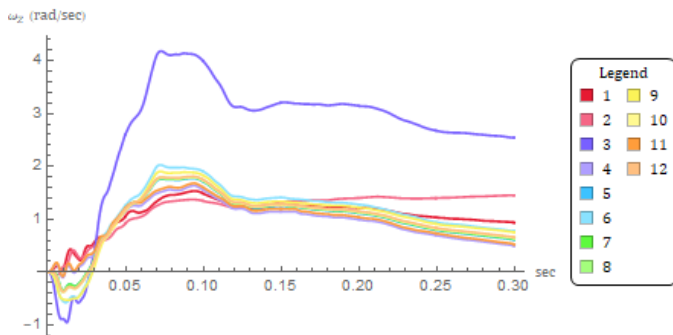


Fig -6: Angular velocity time histories.

For all cases, the angular velocity is positively valued after ~30 milliseconds and remains positive throughout the remainder of the time series. All cases exhibit a peak response before 100 milliseconds, followed by an approximate plateau region and then a negatively sloped region. For all cases, except for case three, the terminus value is less than the peak value. All cases, except for case three, exhibit a peak angular velocity of ~2 rad/sec or less. Including this case, the peak value for the angular velocity is  $1.95 \pm 0.72$  (mean  $\pm$  standard deviation) rad/sec, occurring at  $106 \pm 72.0$  milliseconds (case three with 4.18 rad/sec occurring at 72.9 milliseconds). Excluding this case, the peak value for the angular velocity is  $1.74 \pm 0.16$  rad/sec, occurring at  $108 \pm 63.7$  milliseconds (case six with 2.03 rad/sec occurring at 72.4 milliseconds).

The angular position can again be characterized, in regards to its initial aspect, using a binary descriptive system. An initial negative valuation is observed for the cases in which the y-axis accelerometer at location one is not employed. Regardless of the initial response, the response turns to positive valuation and remains so for the duration of the event. Case three is again an apparent outlier in regards to the magnitude of positive valued angular position after approximately 50 milliseconds. The results are shown in Figure 7. All peak values occur at 299 milliseconds (the terminus of the available data). Including case three, the maximum angular position is  $0.354 \pm 0.144$  radians (case three with a maximum value of 0.807 radians). Excluding this case, the maximum angular position is  $0.313 \pm 0.0210$  radians (case two with a value of 0.355 radians).

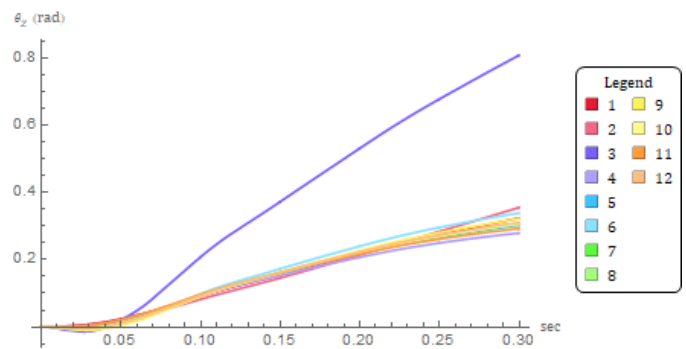


Fig -7: Angular position time histories.

#### 4.2 Body frame translational kinematics

For the body frame translational acceleration responses, cases one-three are not included given that they use the static center of mass accelerometer in their formulation and because body frame fixed points reference the static center of mass location as the origin. The results for the determined time histories for the acceleration along the x-axis and y-axis are shown in Figures 8 and 9, respectively.

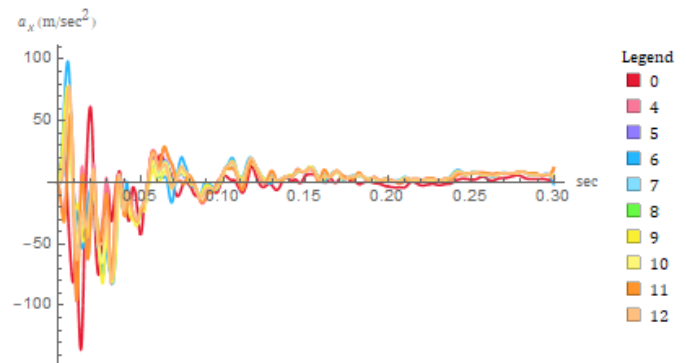


Fig -8: Translational x-axis acceleration time histories.

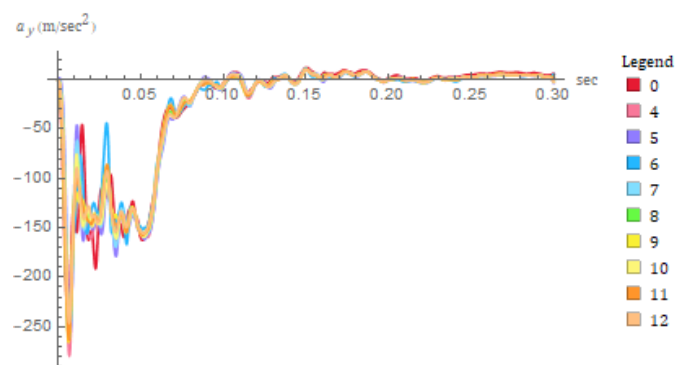


Fig -9: Translational y-axis acceleration time histories.

For the body frame expressed velocity and displacement responses, the measured acceleration at the static center of mass is numerically integrated. For cases one-three, the body frame center of mass acceleration is transformed into components along the inertial frame axes, integrated and then transformed back into body frame coordinates. The results are shown in Figures 10 and 11 for the x-axis and y-axis velocity responses.

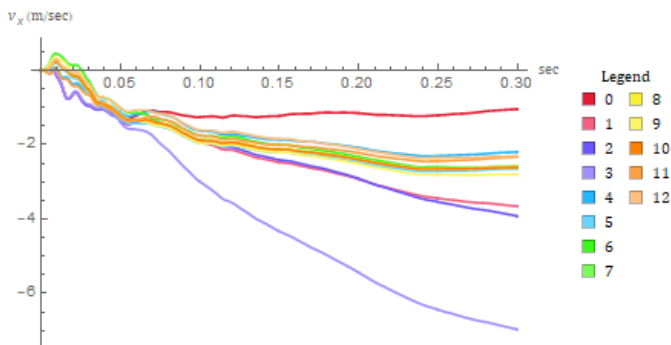


Fig -10: Translational x-axis velocity time histories.

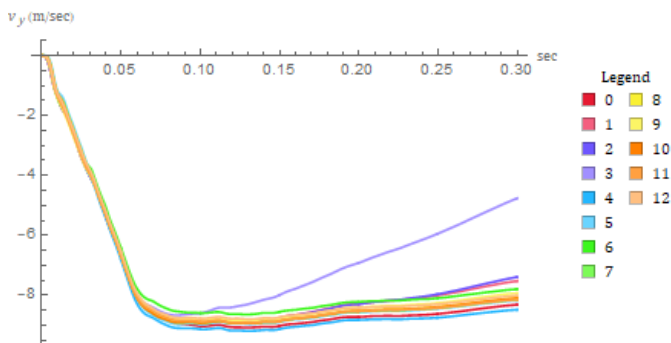


Fig -11: Translational y-axis velocity time histories.

For the velocity components mapped to the x-axis, direct integration of the x-axis static center of mass acceleration reveals and initial positive result, peaking at  $8.47 \cdot 10^{-2}$  m/sec at 5.3 milliseconds, followed by turning negative. The response crosses a zero valuation at between 7.8 and 7.9 milliseconds and remains negative for the remainder of the response. The terminus velocity is -1.04 m/sec. For cases one-three, the initial short-duration positive valuation followed by a turn to a negative valuation is again observed. The magnitude of the terminus negative valued velocity for all three cases is greater than that for case zero and for the other cases. Case three appears to represent an outlier with a terminus velocity of -6.97 m/sec. Including this case, the terminus velocity for cases one-three is  $-4.85 \pm 1.84$  m/sec. Excluding case three, the terminus value was  $-3.79 \pm 0.19$  m/sec. For cases 4-7, the initial response is positive for all cases except for case four. The terminus value for these cases is  $-2.50 \pm 0.211$  m/sec. For cases eight-12, the initial response is positive valued for all cases except for case 11. The terminus value for these cases is determined to be  $-2.52 \pm 0.237$  m/sec. Treating each of the four methods as variants of a single qualitative predictor variable, a linear analysis of variance analysis (ANOVA) reveals that the choice of method is statistically significant in regards to the terminus value ( $p$ -value  $\sim 0.01$ ).

For the velocity components mapped to the y-axis, the sign of the velocity values is negative for the duration of the event (after  $t = 0$ ). Morphologically, each response follows a sequential tripartite form consisting of an initial linear decreasing region, a curved region reaching a minimum

value for the response and a final approximately linear region with a positive slope. For the integration of the y-axis accelerometer at the static center of mass, the minimum velocity is -9.08 m/sec, occurring at 128.7 milliseconds, and the terminus velocity is -8.31 m/sec. Case three again represents an outlier in regards to terminus value (-4.76 m/sec). Including this case for cases one-three, the minimum value is  $-8.82 \pm 0.14$  m/sec, occurring at  $95.4 \pm 9.3$  milliseconds. The terminus value is  $-6.55 \pm 1.56$  m/sec. Excluding this case for cases one-three, the minimum value is  $-8.90 \pm 0.01$  m/sec, occurring at  $100.8 \pm 0.1$  milliseconds and with a terminus value of  $-7.45 \pm 0.09$  m/sec. For cases four-seven, the minimum value is  $-8.93 \pm 0.22$  m/sec, occurring at  $122.8 \pm 14.3$  milliseconds. The terminus value for these cases is  $-8.15 \pm 0.28$  m/sec. For cases eight-12, the minimum value is  $-8.88 \pm 0.06$  m/sec, occurring at  $130.1 \pm 0.9$  m/sec and with a terminus value of  $-8.05 \pm 0.09$  m/sec. The choice of modeling methodology is borderline in regards to statistical significance ( $p$ -value  $\sim 0.07$ ).

The results for the body frame axes mapped displacement components are shown in Figures 12 and 13.

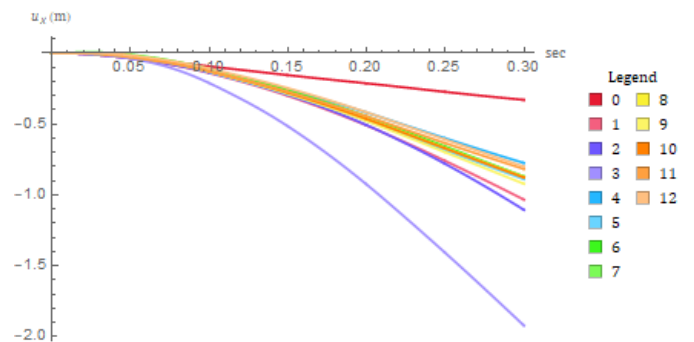


Fig -12: Translational x-axis displacement time histories.

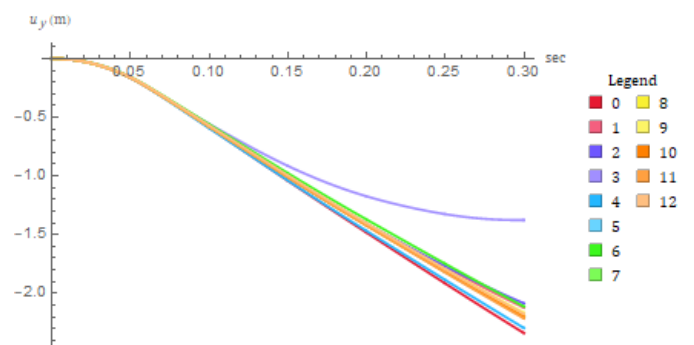


Fig -13: Translational y-axis displacement time histories.

For the x-axis displacement, all cases follow a biphasic morphology consisting of an initial duration of zero valuation followed by negative valued displacement for the remainder of the event. For the displacement based upon integration of the x-axis static center of mass accelerometer, the initial response ( $< 1$  mm) is present for 13.7 milliseconds. The terminus value is -0.33 m. The terminus response for all of the other cases is greater

valued, in magnitude, than this baseline case. Case three again is an outlier with a terminus value of  $-1.92$  m. Including this case in cases one-three, the terminus displacement is  $-1.35 \pm 0.49$  m, while excluding this case results in a terminus displacement of  $-1.07 \pm 0.05$  m. For cases four-seven, the terminus displacement is  $-0.85 \pm 0.05$  m. For cases eight-12, the terminus displacement is  $-0.86 \pm 0.05$  m. The choice of methodology is statistically significant ( $p$ -value  $\sim 0.02$ ).

For the  $y$ -axis displacement, the response morphology mirrors the  $x$ -axis displacement morphology. For the displacement based upon integration of the  $y$ -axis static center of mass accelerometer, the initial response ( $< 1$  mm) is present for 5.8 milliseconds. The terminus displacement for this case is  $-2.34$  m. Case three continues to be an outlier with a terminus displacement of  $-1.38$  m. For cases one-three, inclusion of this case results in a terminus displacement of  $-1.86 \pm 0.42$  m. Excluding this case in cases one-three results in a terminus displacement of  $-2.10 \pm 0.03$  m. For cases four-seven, the terminus displacement is  $-2.20 \pm 0.08$  m. For cases eight-12, the terminus displacement is  $-2.19 \pm 0.02$  m. The choice of methodology is not statistically significant ( $p$ -value  $\sim 0.13$ ).

### 4.3 Inertial frame translational kinematics

For the inertial frame translational kinematic responses, case zero is not included and could not be included given the fact that the DCM for vector component transformation from the body frame to the inertial frame was not available. The  $X$ -axis and  $Y$ -axis responses are shown in Figures 14 and 15, respectively.

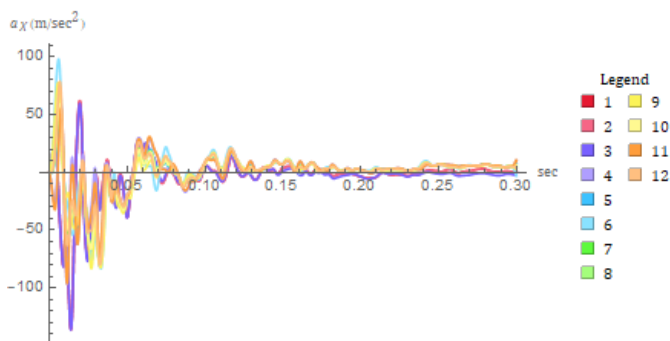


Fig -14: Translational X-axis acceleration time histories.

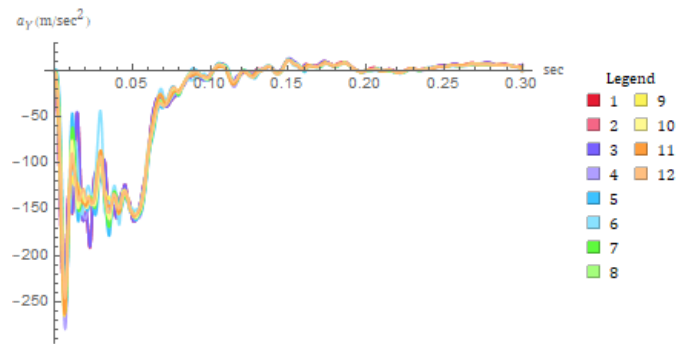


Fig -15: Translational Y-axis acceleration time histories.

The inertial frame mapped velocity responses are shown in Figure 16 and 17.

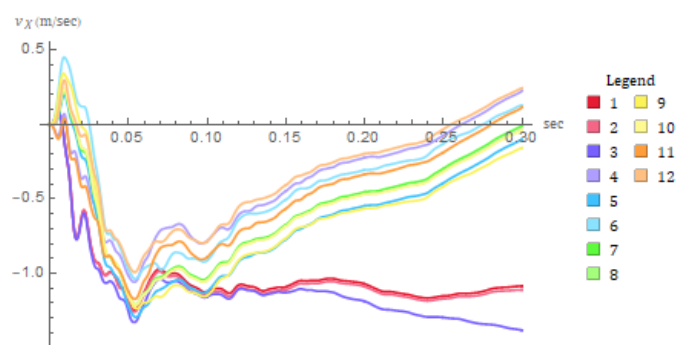


Fig -16: Translational X-axis velocity time histories.

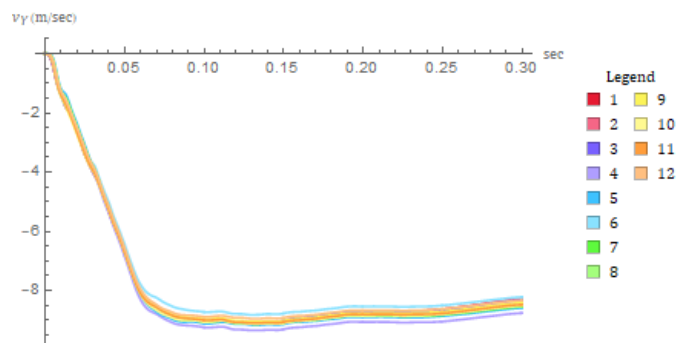


Fig -17: Translational Y-axis velocity time histories.

For the  $X$ -axis velocity response, cases one-three exhibit an initial positive valued response followed by a rapid turn into negative valued velocities. The response for these three cases is morphologically different than the other cases. For cases one and two, the terminus region of the response, after reaching a peak negative value, is a region of increasing slope followed by an approximate flat response with a terminus approximate 50 millisecond response with a slight positive slope. For case three, the response diverges from the other two cases at approximately 120 milliseconds and with a terminus negative slope. For this case, the peak negative velocity, of  $-1.38$  m/sec, occurs at the terminus of the signal. Excluding this case, the peak negative velocity is  $-1.25 \pm 0.01$  m/sec, occurring at  $53.7 \pm 0.0$  milliseconds. The terminus value is  $-1.10 \pm 0.02$  m/sec. For all other cases (i.e. cases four-12), the velocity response after

approximately 100 milliseconds is positive sloped. For cases four-seven, the peak negative velocity is  $-1.15 \pm 0.12$  m/sec, occurring at  $54.3 \pm 0.0$  milliseconds. The terminus velocity for these cases is  $0.06 \pm 0.14$  m/sec. For cases eight-12, the peak negative velocity is  $-1.16 \pm 0.10$  m/sec, occurring at  $54.4 \pm 0.0$  milliseconds. The terminus velocity for these cases is  $0.03 \pm 0.16$  m/sec. The choice of method is statistically significant ( $p \sim 0$ ).

The Y-axis velocity response morphologically mirrors the normative y-axis (i.e. excluding case three for the latter) response. For cases one-three, the peak negative response is  $-9.08 \pm 0.01$  m/sec, occurring at  $128.9 \pm 0.0$  milliseconds. The terminus response is  $-8.30 \pm 0.02$  m/sec. For cases four-seven, the peak negative response is  $-9.11 \pm 0.22$  m/sec, occurring at  $131.8 \pm 0.0$  milliseconds. The terminus response is  $-8.52 \pm 0.23$  m/sec. For cases eight-12, the peak negative response is  $-9.07 \pm 0.07$  m/sec, occurring at  $132.6 \pm 0.0$  milliseconds. The terminus response is  $-8.44 \pm 0.07$  m/sec. The choice of method is not statistically significant ( $p \sim 0.16$ ).

The inertial frame mapped displacement responses are shown in Figure 18 and 19.

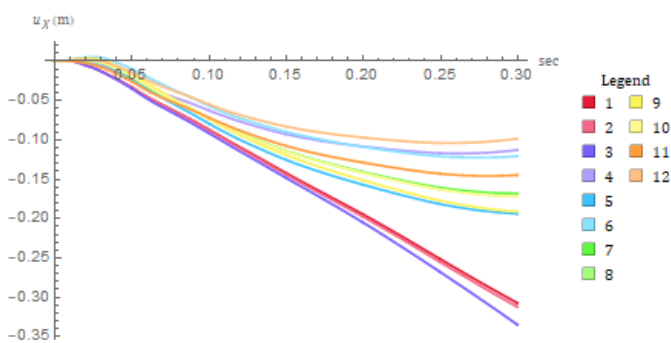


Fig -18: Translational X-axis displacement time histories.

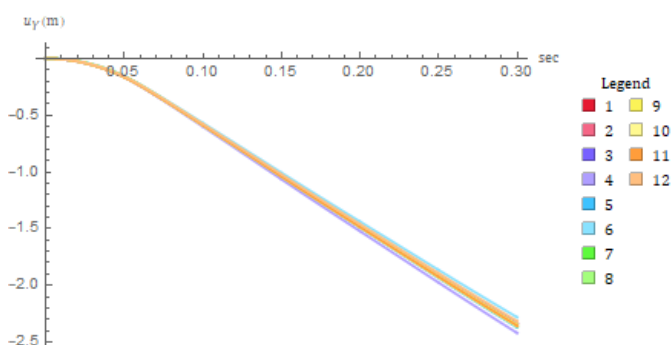


Fig -19: Translational Y-axis displacement time histories.

The displacements for both axes mirror the corresponding velocity responses. For the X-axis, cases one-three again differ from the other cases. The initial negative slope is steeper than for the other cases. The terminus response slope is negative for all three cases while the terminus response for the other cases is curved and with the response towards the point of flattening. The terminus responses are all negatively valued and with a peak

magnitude occurring at the terminus of the response. For cases one-three, the terminus displacement is  $-0.318 \pm 0.01$  m. For cases four-seven, the terminus displacement is  $-0.149 \pm 0.04$  m. For cases eight-12, the terminus displacement is  $-0.156 \pm 0.04$  m. The choice of method is statistically significant ( $p \sim 1.4 \cdot 10^{-4}$ ).

For the Y-axis displacement response, the terminus responses are all negatively valued and are the peak negative responses for each case. For cases one-three, the terminus displacement is  $-2.34 \pm 0.00$  m. For cases four-seven, the terminus displacement is  $-2.36 \pm 0.06$  m. For cases eight-12, the terminus displacement is  $-2.35 \pm 0.02$  m. The choice of method is not statistically significant ( $p \sim 0.8$ ).

#### 4.4 Dynamic time warping analysis

The warping distance results are summarized in Tables 2-4.

Table -2: DTW distances for the angular kinematic response parameters. The case numbers are parenthetically shown.

Param.	Mean	SD	Min	Max
$\theta_z$	111.1	205.5	$5.277 \cdot 10^{-1}$ (8 & 10)	613.3 (3 & 4)
$\omega_z$	1074	1763	2.958 (8 & 10)	5383 (3 & 4)
$\alpha_z$	$1.220 \cdot 10^4$	$1.220 \cdot 10^4$	190.7 (8 & 12)	$3.858 \cdot 10^4$ (2 & 3)

Table -3: DTW distances for the body frame kinematic response parameters. The case numbers are parenthetically shown.

Param.	Mean	SD	Min	Max
$a_x$	$6.310 \cdot 10^4$	$4.715 \cdot 10^4$	63.52 (8 & 10)	$1.612 \cdot 10^4$ (0 & 9)
$v_x$	1564	1965	7.419 (8 & 10)	8691 (0 & 3)
$u_x$	204.8	283.8	$6.618 \cdot 10^{-1}$ (8 & 10)	1440 (0 & 3)
$a_y$	$3.725 \cdot 10^4$	$1.786 \cdot 10^4$	929.1 (9 & 11)	$7.310 \cdot 10^4$ (0 & 6)
$v_y$	672.0	949.4	14.47 (7 & 10)	3879 (3 & 4)
$u_y$	88.11	172.3	$8.684 \cdot 10^4$ (8 & 10)	599.3 (0 & 3)

Table -4: DTW distances for the inertial frame kinematic response parameters. The case numbers are parenthetically shown.

Param.	Mean	SD	Min	Max
$a_x$	9124	6400	105.3 (8 & 10)	$2.074 \cdot 10^4$ (3 & 9)
$v_x$	728.8	712.2	1.415 (8 & 10)	2199 (3 & 12)
$u_x$	93.75	66.42	$3.495 \cdot 10^{-1}$ (3 & 10)	247.1 (3 & 12)
$a_y$	3886	1692	75.28 (1 & 2)	$6.371 \cdot 10^4$ (2 & 6)

$v_y$	208.2	196.4	1.679 (1 & 2)	1110 (4 & 6)
$u_y$	6.576	6.181	$4.652 \cdot 10^{-1}$ (1 & 2)	31.15 (4 & 6)

In virtually all cases, the WarpingCorrespondence function in Mathematica extends the signal length beyond the original 3000 samples. For each comparison, both signals are extended by the same length. Using  $u_y$  as an example, the cases corresponding to the minimum value (cases one and two) are not extended while the cases corresponding to the maximum value (cases four and six) are extended by 162 data points. This latter case is shown in Figure 20.

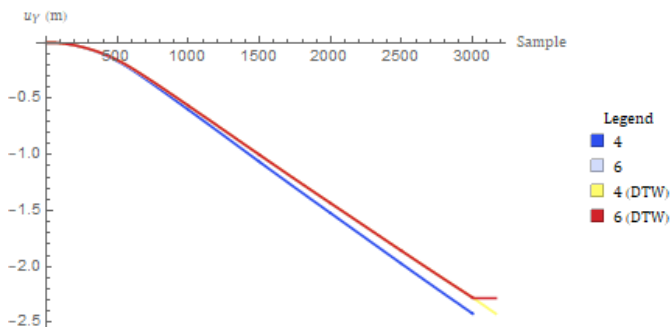


Fig -20: Cases four & six and their DTW signals for  $u_y$ .

The results of the  $L_1$  norms of the DTW signal differences, normalized to the  $L_1$  norm of the first DTW signal in the difference, expressed as percentages, are shown in Tables 5-7. It should be clear that for any cases  $\{a, b\}$ , the normalized difference depends on the vector used for normalization (unless  $a = b$ ).

Table -5: Normalized  $L_1$  percentage differences for the angular kinematic response. The case numbers are parenthetically shown and with the first case being the reference case.

Param.	Mean	SD	Min	Max
$\theta_z$	7.077	14.20	$1.949 \cdot 10^{-2}$ (8 & 10)	53.69 (3 & 4)
$\omega_z$	18.84	33.71	$4.477 \cdot 10^{-2}$ (8 & 10)	145.1 (3 & 4)
$\alpha_z$	18.50	12.66	$4.649 \cdot 10^{-1}$ (12 & 8)	47.75 (3 & 2)

Table -6: Normalized  $L_1$  percentage differences for the body frame kinematic response. The case numbers are parenthetically shown and with the first case being the reference case.

Param.	Mean	SD	Min	Max
$a_x$	13.73	10.02	$1.995 \cdot 10^{-1}$ (10 & 8)	35.46 (0 & 9)
$v_x$	18.42	25.73	$3.837 \cdot 10^{-2}$ (8 & 10)	206.1 (3 & 0)
$u_x$	10.49	16.78	$2.228 \cdot 10^{-2}$ (8 & 10)	123.7 (3 & 0)
$a_y$	2.672	1.143	$7.722 \cdot 10^{-1}$ (11 & 9)	4.958 (0 & 6)
$v_y$	1.632	2.503	$2.187 \cdot 10^{-2}$	9.873

			(10 & 7)	(4 & 3)
$u_y$	1.865	3.931	$1.860 \cdot 10^{-1}$ (8 & 7)	14.09 (0 & 3)

Table -7: Normalized  $L_1$  percentage differences for the inertial frame kinematic response. The case numbers are parenthetically shown and with the first case being the reference case.

Param.	Mean	SD	Min	Max
$a_x$	20.90	14.64	$3.284 \cdot 10^{-1}$ (10 & 8)	48.70 (3 & 9)
$v_x$	24.81	33.12	$3.526 \cdot 10^{-2}$ (8 & 10)	155.5 (3 & 12)
$u_x$	14.88	12.75	$1.964 \cdot 10^{-2}$ (8 & 10)	60.43 (3 & 12)
$a_y$	2.717	1.080	$7.441 \cdot 10^{-2}$ (2 & 1)	4.317 (2 & 6)
$v_y$	$3.475 \cdot 10^{-1}$	$4.080 \cdot 10^{-1}$	$4.464 \cdot 10^{-3}$ (2 & 1)	2.449 (4 & 6)
$u_y$	$5.636 \cdot 10^{-2}$	$5.504 \cdot 10^{-2}$	$1.470 \cdot 10^{-2}$ (2 & 1)	$3.388 \cdot 10^{-1}$ (4 & 6)

#### 4.5 Videogrammetry analysis

The wide view overhead collision test video starts at 50 milliseconds prior to the start of the collision (frame number -50). Each frame represents a one millisecond advancement in the incident sequence. Deformation of the left side of the test vehicle and the front of the MDB are observable after the start of closure ( $t = 0$ ) and prior to any discernable gross movement of the test vehicle. The first perceptible movement of the test vehicle appears to be of rolling to the right (i.e. negative rotation about the  $x$ -axis of the test vehicle). As the collision proceeds, the test vehicle translates negatively along both planar inertial reference frame axes and rotates counterclockwise in yaw. The terminus of the separation phase is difficult to ascertain from the video due to the presence of debris from the left side of the vehicle obscuring the collision interface. Examination of the other available collision test videos shows that the terminus of the separation phase occurs within the vicinity of 100 milliseconds. A subset of the tracker locations are shown in Figure 21. Figure 22 shows the corresponding mapped vehicle model mesh.

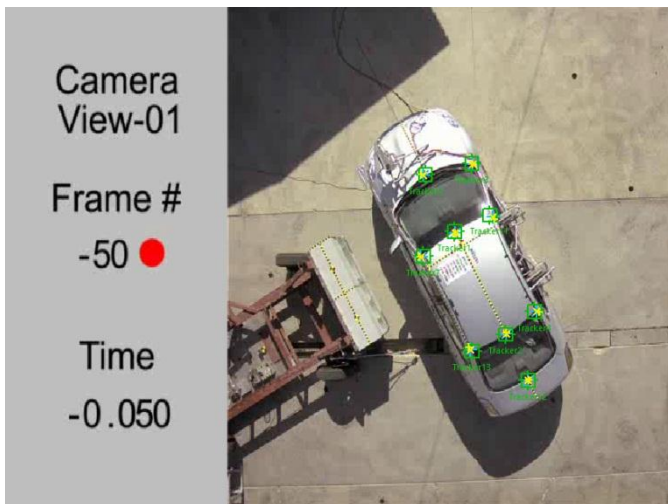


Fig -21: Tracker locations at -50milliseconds.



Fig -24: Vehicle mesh mapped at 100 milliseconds.

Finally, Figures 25 and 26 depict the tracker locations and mapped vehicle model mesh at the terminus of the video recording.



Fig -22: Vehicle mesh mapped at -50 milliseconds.

Figures 23 and 24 show the trackers and the mapped vehicle mesh at 100 milliseconds.

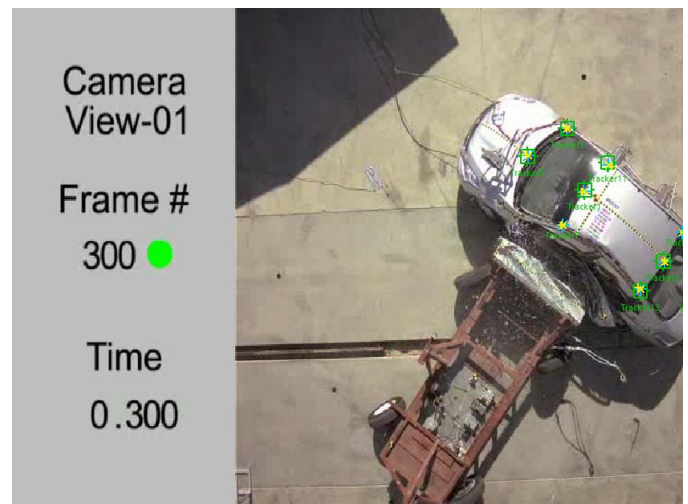


Fig -25: Tracker locations at 300 milliseconds.

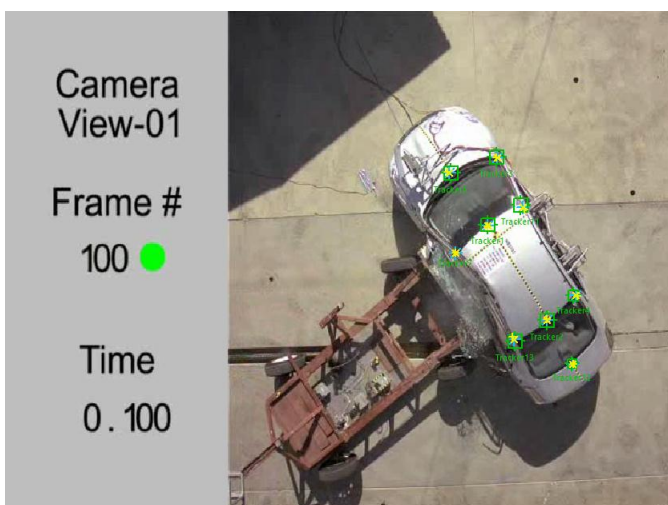


Fig -23: Tracker locations at 100 milliseconds.



Fig -26: Vehicle mesh mapped at 300 milliseconds.

The software follows the naming convention of tilt-roll-pan, consistent with camera terminology, for the corresponding names of pitch-roll-yaw in regards to vehicle dynamics. The pan (yaw) response was the one that was consistent with the subject planar analysis. The time history of the response, as shown in Figure 27, is one of a short duration near zero-valued response, followed by a short duration negative valued response and with the majority of the response being positive. The angular position at 299 milliseconds, corresponding to maximum post-start of impact time value for the instrumentation data, is 0.387 radians. The inertial frame X-axis response consists of an initial near zero valued response followed by a negative magnitude response. The X-axis position at 299 milliseconds is -0.555 m. The inertial frame Y-axis response consists of an initial short duration near zero response followed by a short duration positive response and with the remainder of the response being negative valued. The Y-axis position at 299 milliseconds is -1.75 m. These time histories are shown in Figure 28.

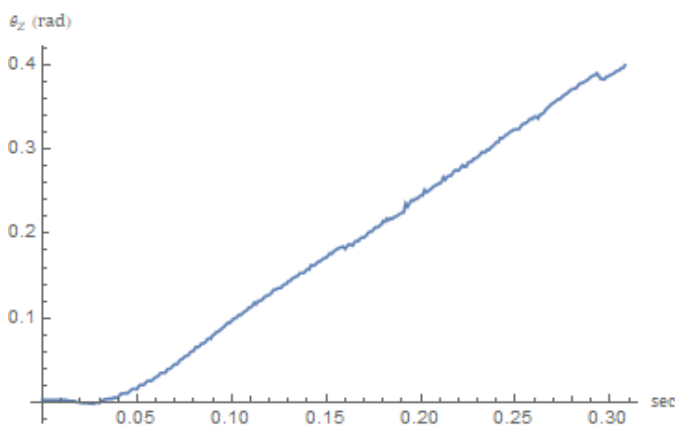


Fig -27: Videogrammetry based angular position time history.

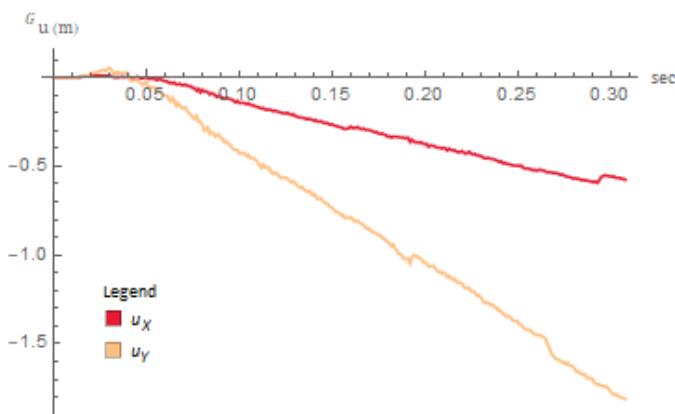


Fig -28: Videogrammetry based inertial frame of reference planar position time-histories.

#### 4.6 3d based reconstruction of $\theta_z$

The results of the determination of the time histories of the three components of the angular position of the body

frame, about the inertial frame of reference, expressed in terms of the inertial frame of reference, are shown in Figure 29.

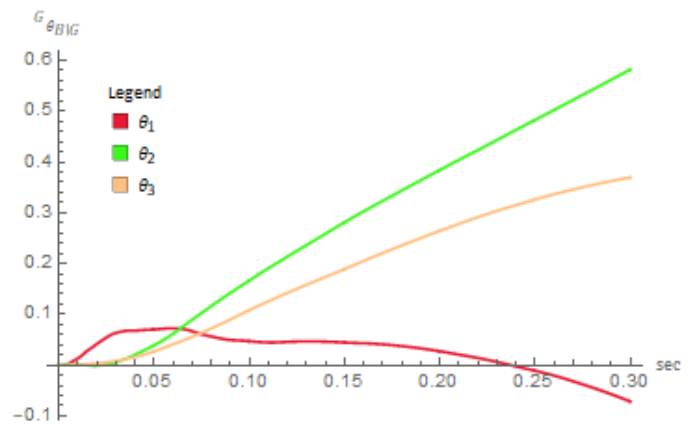


Fig -29: Angular position component time histories.

The terminus value, as shown per the plot labeled  $\theta_3$ , in Figure 29, is 0.370 radians. Figure 30 shows the composite plot of Figures 7, 27 and the  $\theta_3$  plot from Figure 29.

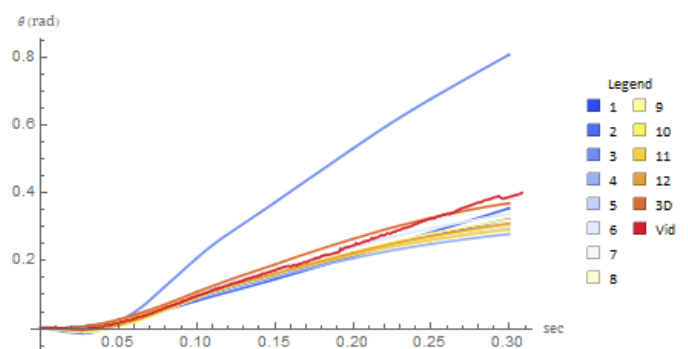


Fig -30: Composite angular position time history plot.

### 5. DISCUSSION & CONCLUSIONS

The context of the subject application, that being a deformable barrier striking the side of a deformable test vehicle, by definition, involves an impact between two objects that are strictly non-rigid. Beyond simple semantics, this can readily be seen in regards to the test case that is considered for the subject work. For the test vehicle, depending on height and longitudinal location, the maximum depth of residual damage over the directly impacted area is between 200 and 280 mm. For the MDB, under the same conditions and caveats, the maximum depth of residual damage is between 150 and 175 mm. The deformable nature of the collision partners, however, does not and did not preclude the application of rigid body dynamics theory for the purpose of elucidating the rigid body translational and rotational modes that are operative during the collision.

The rigid body theory presented in Section 2 is apt for any rigid body dynamics problem and is not limited to the

subject collision context. There are, however, a number of context specific points and evaluated test specific points that merit mention.

The first is that the static center of mass of the test vehicle was taken as the dynamic center of mass of the same. Given the deformation of the test vehicle, one might reasonably expect at least a lateral shift (along the  $-y$ -axis of the test vehicle), dynamically, of the center of mass of the test vehicle during the collision. The extent to which such occurred and the impact of such an occurrence are beyond the scope of the subject study.

A second point is that the choice of accelerometers and accelerometer block sensing axes play an important role in regards to the determination of the rigid body kinematic response. From Figure 2, it is readily apparent that the peripheral  $x$ -axis accelerometers lag the static center of mass  $x$ -axis acceleration in regards to the first large negative peak and are of lower magnitude. More obvious is the difference in the  $y$ -axis acceleration response, as per Figure 3, at location three. It is this sensing axis, at this location, that produces an outlier response in both the angular and body frame translational kinematics, as is clear by examination of Figures 5-13. The underlying issue with the sensing axis in question is not known. However, the extent to which this sensing axis impacts the response is mitigated for those cases that involve additional accelerometer locations and sensing axes (e.g. cases 5-10 and 12). Excluding case three, the body frame expressed  $y$ -axis displacement and velocity represented situations in which the reconstructed responses produced a closer match to the numerically integrated static center of mass response when compared with the situation for the  $x$ -axis. A potential cause for this might be the locations of the available peripheral accelerometer blocks located outside of the region of direct impact. For example, comparing the locations of peripheral sensing blocks one and two, the  $x$ -axis locations span the location of the static center of mass while the  $y$ -axis locations are both to the right of the  $x$ -axis and separated by a mere 3 mm. The translational  $Y$ -axis displacement and velocity responses, correspondingly with respect to the body-frame responses, fit within a relatively narrow band. The  $X$ -axis responses exhibit substantial deviation. This is most clearly observed in the velocity response as per Figure 16, which in turn, is mirrored in the displacement response of Figure 18. Accelerometer positioning, leading to the differences observed in the body frame response, thereby leading to a difference in the transformed (into the inertial frame for relatively low angular displacement) response, is the most likely cause (over other potential issues such as accelerometer drift).

A third point of import is that a potential source for error lies within the digital signal filtering approach used herein. It is important to note that the use of CFC filters is based upon the SAE J211 standard. In theory, all accelerometers should be zeroed prior to and at time  $t = 0$ . In the

experience of the author, this is rarely the case. For the subject case, as an example, the test vehicle static center of mass unfiltered  $x$ -axis accelerometer data, prior to  $t = 0$ , exhibits an asymmetric noise signal that ranges from  $+0.4G$  to  $-0.3G$ . This issue is compounded by the following two factors. The first is that the frequency composition of the known component of the noise signal (i.e. the time domain component of the signal prior to  $t = 0$ ) tends to overlap the frequency response of the signal after and including  $t = 0$ . The second is that the difference equation for the CFC filter can result in filter generated non-zero valued time domain artifacts, especially in regions with high magnitude slope changes. This occurs because the difference equation for the filtered response, at discrete time  $t$ , is based on the unfiltered data at time  $t$ ,  $t - 1$  and  $t - 2$  as well as the filtered response at  $t - 1$  and  $t - 2$ . The establishment of standards for alternative filtering methods, such as wavelet based filtering, do not exist as of the time of the writing of the subject work.

The relationship between the terminus kinematic responses and methodology (i.e. the composition of the accelerometer sensing blocks used) was evaluated using a single factor ANOVA statistical test for a single indexed variable. While useful, it should be noted that the assumptions for this test include, but are not limited to, each sample group being normally distributed, all populations having a common variance and all samples being drawn independently. The use of data from a given sensor block sensing axis for multiple compositions clearly stretches the boundaries of these assumptions. The determination of the DTW distances and normalized  $L_1$  norm differences mirrors the observable differences for each response parameter. It should be noted that these metrics are relative on a pairwise basis, for each method, and not with respect to a given or fixed standard.

The videogrammetry and  $\square^3$  analyses were conducted to generate results against which the results of the planar analyses could be compared with and contrasted against. There has been rather limited literature-based reporting on the use of video based methods for analyzing the dynamics and kinematics of controlled collision testing. Wang and Gabler (2007) indicated that 'motion analysis software' was used to track the frame-by-frame motion of a single door fixed marker, per collision test, in the analysis of high speed video footage from front impact NCAP data [33]. The authors, however, did not provide any reporting for the employed methodology, if actually used, for mitigating camera vibration and correcting for lens distortion. Martins et al. (2016) presented a simplified method for single frame image correction based upon a known dimension of an object within the frame [34]. Rose et al. (2016) presented a data plot showing the estimated yaw rate time history for their evaluation of NHTSA test no. 5832 (lateral NCAP testing for a 2007 Hyundai Santa Fe utility vehicle) [35]. This figure (Figure 7 of the reference) appears to show eight data points with

the initial data point at between 25 and 50 milliseconds (data value of slightly under 40 degrees/second), a peak value of approximately 80 degrees/second at near 100 milliseconds and a terminus response occurring at slightly before 350 milliseconds. This data was generated by determining the frame-to-frame change in the yaw angle, using CAD software, and without lens distortion correction [36]. The following additional analysis was undertaken to obtain a general comparison of the results from cited work with the results of the subject work (analysis not shown). The figure from a digital copy of this reference was imported and the color channel information was used to segment the image and thereby extract the data from the figure. A Gaussian filter was applied to the resultant image followed by binarization and color negation. The resultant non-zero valued image data was then geometrically transformed using the known positions of the figure origin, terminus of x-axis and terminus of y-axis. This data was interpolated and then the resulting function was integrated. The resulting angular displacement, at a time value of 299 milliseconds, was determined to be 0.305 radians (17.47 degrees).

The use of videogrammetry in which video object based trackers, linked to a geometrically accurate mesh model, for determining the kinematic response of the underlying object, appears to be a novel implementation, solely in regards to context. The terminus angular position, based upon the videogrammetry analysis, is 0.387 radians (22.2 degrees). Excluding case three, this is slightly greater than the planar accelerometer based solutions ( $0.313 \pm 0.0210$  radians;  $17.9 \pm 1.21$  degrees). The inertial frame **X** and **Y** axis position (displacement with respect to zero) values at 299 milliseconds are -0.555 m and -1.75 m, respectively. Excluding case three, the corresponding accelerometer based solutions are  $-0.181 \pm 0.0701$  m and  $-2.35 \pm 0.0342$  m. Additional work is required, inclusive of using linked videos from multiple camera angles, to determine if the videogrammetry based data can be refined.

The extent of the analysis in  $\square^3$  was the determination of the predicted angular position in regards to the **Z**-axis. The transformation from the body frame expression of the angular kinematics into the inertial frame was necessary due to the fact that the **z**-axis of the test vehicle and the **Z**-axis of the inertial frame of reference do not remain coincident, generally, for the non-planar case. The quantified angular position at 299 milliseconds, of 0.370 radians, is between the mean value determined from the accelerometer based approaches and the value determined from the videogrammetry analysis. Clearly, additional work can readily be performed to extend the  $\square^3$  analysis to elucidate the full kinematic response.

It should be remembered that the kinematic response of the test vehicle arises from the presence of the net sum of externally applied loads that are unbalanced. The collision force, while predominate, is not the sole force. The other forces of relevance include the force from the gravity of

the Earth, tire forces and suspension forces. As the vehicle body undergoes triaxial rotation, about the suspension of the test vehicle, the lateral and longitudinal sensing axes of the accelerometers attached to the body of the test vehicle record acceleration components due the sum of all loads on the vehicle body. This includes the components of gravitational acceleration that map along these axes. These components are vectorially additive to the relevant components of the acceleration engendered due to the force of the collision but are additive either positively or negatively, as a function of the orientation of the vehicle body with respect to the inertial frame of reference. Excluding the sensor locations within the region of direct impact, there exists only one other sensing axis, at location six, outside of the three peripheral triaxial sensor blocks, that could be used if the triaxial sensor block at the static center of mass is not used. This precludes the use of the minimum 12 sensing axis formulation that was developed in the subject work. Other implementations such as the 3-3-3 configuration [17], relying on a least squares formulation, could be considered.

The subject work, in regards to the example considered, focused on the presentation of the kinematic results of the test vehicle. A full system dynamics evaluation would clearly require an evaluation of the kinematic response of the MDB followed by an evaluation of the translational and rotational system dynamics. In this regard, it is important to recall that Newton's laws of mechanics are valid in an inertial frame of reference. The relevant MDB instrumentation consists of one triaxial sensor block and one biaxial sensor block. This allows for a planar implementation for the MDB kinematics but not for a fully deterministic general motion formulation. A preliminary planar accelerometer based evaluation for the MDB (analysis not shown) reveals that the MDB undergoes a change in angular position, about the **Z**-axis, from  $-0.5\pi$  radians ( $-1.57$  radians;  $-90$  degrees) to  $-1.245$  radians ( $-71.3$  degrees), representing a positive angular displacement of 0.33 radians (18.7 degrees). The direction of rotation, that being counterclockwise planar rotation of the MDB, is readily validated by comparing the MDB angular positions between Figures 21, 23 and 25.

## ACKNOWLEDGEMENT

Acknowledgement is due to Nicholas Carpenter, PhD, of Collision Dynamics Analysis. The discussions between Dr. Carpenter and the subject author, during the early part of the latter's career, served as the impetus for the subject work.

## REFERENCES

- [1] J. Morris (1973) "Accelerometry – a technique for the measurement of human body motions." *J. Biomechanics* 6: 729-736.

- [2] A. Padgaonkar, K. Krieger and A. King (1975) "Measurement of angular acceleration of a rigid body using linear accelerometers." *J. Applied Mechanics* 42(3): 552-556.
- [3] C. Chou and S. Sinha (1976) "On the kinematics of the head using linear acceleration measurements." *J. Biomechanics* 9: 607-613.
- [4] W. Hayes, J. Gran, M. Nagurka, J. Feldman and C. Oatis (1983) "Leg motion analysis during gait by multiaxial accelerometry." *J. Biomechanical Engineering* 105: 283-289.
- [5] J. Cholewicki, M. Panjabi, K. Nibu, L. Babat, J. Grauer and J. Dvorak (1998) "Head kinematics during in vitro whiplash simulation." *Accident Analysis & Prevention* 30(4): 469-479.
- [6] F. Luan, H. Yang, B. Deng, P. Begeman, S. Tashman and A. King (2000) "Qualitative analysis of neck kinematics during low-speed rear-end impacts." *Clinical Biomechanics* 15(9): 649-657.
- [7] J. Beckwith, J. Chu and R. Greenwald (2007) "Validation of a noninvasive system for measuring head acceleration for use during boxing competition." *J. Applied Biomechanics* 23: 238-244.
- [8] G. Nusholtz and R. Molinaro (1991) "Force deflection curves for airbag response." *Experimental Techniques* March/April: 33-35.
- [9] G. Nusholtz, J. Wu and P. Kaiker (1991) "Passenger airbag study using geometric analysis of rigid-body motion." *Experimental Mechanics* 31(3): 264-270.
- [10] R. Shea and D. Viano (1994) "Computing body segment trajectories in the Hybrid III dummy using linear accelerometer data." *J. Biomechanical Engineering* 105: 283-289.
- [11] M. Costello and C. Webb (2005) "Angular rate estimation using fixed and vibrating triaxial acceleration measurements." *J. Spacecraft and Rockets* 42(6): 1133-1137.
- [12] G. Nusholtz (1993) "Geometric methods in determining rigid-body dynamics." *Experimental Mechanics* 31(3): 264-270.
- [13] P. Cardou, G. Fournier and P. Gagnon (2011) "A nonlinear program for angular-velocity estimation from centripetal acceleration measurements." *IEEE/ASME Transactions on Mechatronics* 16(5): 932-944.
- [14] N. Mital and A. King (1979) "Computation of rigid-body rotation in three-dimensional space from body-fixed linear acceleration measurements." *J. Applied Mechanics* 46: 925-930.
- [15] F. DiMasi (1996) "Transformation of nine-accelerometer package (NAP) data for replicating headpart kinematics and dynamic loading." NHTSA Technical Report, DOT HS 808 282. Springfield, Virginia: National Technical Information Service.
- [16] P. Martin, G. Hall, J. Crandall and W. Pilkey (1998) "Measuring the acceleration of a rigid body." *Shock and Vibration* 5: 211-224.
- [17] N. Alem and G. Holstein (1977) "Measurement of 3-D motion." Presented: 5<sup>th</sup> International Workshop on Human Subjects for Biomechanical Research; New Orleans, Louisiana. Also: University of Michigan Highway Safety Research Institute publication UM-HSRI-77-46.
- [18] P. Cappa, L. Masia and G. Patane (2005) "Numerical validation of linear accelerometer systems for the measurement of head kinematics." *J. Biomechanical Engineering* 127(6): 919-928.
- [19] T. Williams and K. Fyfe (2004) "Planar accelerometer configurations." *J. Applied Mechanics* 71(1): 10-14.
- [20] P. Cheng and D. Guenther (1989) "Effect of angular velocity of a vehicle on the change in velocity experienced by an occupant during a crash environment and localized delta-V concept." Society of Automotive Engineers Technical Paper No. 890636.
- [21] R. Bundorf (1996) "Analysis and calculation of delta-V from crash test data." Society of Automotive Engineers Technical Paper No. 960899.
- [22] B. McHenry and R. McHenry (1997) "RICSAC-97: A reevaluation of the reference set of full scale crash tests." Society of Automotive Engineers Technical Paper No. 970961.
- [23] M. Marine and S. Werner (1998) "Delta-V analysis from crash test data for vehicles with post-impact yaw motion." Society of Automotive Engineers Technical Paper No. 980219.
- [24] D. Struble, K. Welsh and J. Struble (2001) "Side impact structural characterization from FMVSS 214D test data." Society of Automotive Engineers Technical Paper No. 2001-01-0122.
- [25] J. Singh (2013) "A fundamental reconsideration of the CRASH3 damage analysis algorithm: the case against uniform, ubiquitous linearity between BEV, peak collision force magnitude, and residual damage depth." *Traffic Injury Prevention* 14(7): 718-724.
- [26] Laboratory test procedure for FMVSS No. 214, dynamic side impact protection (2012) US Department of Transportation, National Highway Traffic Safety Administration. Enforcement, Office of Vehicle Safety Compliance, Washington, DC.
- [27] Laboratory test procedure for the New Car Assessment Program side impact moving deformable barrier test (2012) US Department of Transportation, National Highway Traffic Safety Administration. Office of Crashworthiness Standards, Washington, DC.
- [28] R. Jazar (2011) *Advanced dynamics: rigid body, multibody and aerospace applications*. Hoboken, New Jersey, USA: John Wiley & Sons, Inc., pp. 718-721.
- [29] S. Park and K. Hong (2011) "Angular rate estimation using a distributed set of accelerometers." *Sensors* 11: 10444-10457.
- [30] Vehicle Crash Test Database. National Highway Traffic Safety Administration. <https://www-nrd.nhtsa.dot.gov/database/VSR/veh/QueryTest.aspx>
- [31] NHTSA NVS Software. National Highway Traffic Safety Administration. <https://www.nhtsa.gov/databases-and-software/signal-analysis-software-windows>
- [32] H. Sarin, M. Kokkolaras, G. Hulbert, P. Papalambros, S. Barat and R.-J. Yang (2010) "Comparing time histories for validation of simulation models: error measures and metrics." *J. of Dynamic Systems, Measurement and Control* 132(6): 061401-1-10.
- [33] Q. Wang and H. Gabler (2007) "Accuracy of vehicle frontal stiffness estimates for crash reconstruction." Paper No. 07-0513. 20<sup>th</sup> International Technical Conference on the Enhanced Safety of Vehicles, Lyon, France; June 18-21.

- [34] J. Martins, R. Ribeiro, P. Neves and F. Brito (2016) "Accident reconstruction using data retrieval from crash-test video images." Society of Automotive Engineers Technical Paper No. 2016-01-1464.
- [35] N. Rose, N. Carter and G. Beauchamp (2016) "Post-impact dynamics for vehicles with a high yaw velocity." Society of Automotive Engineers Technical Paper No. 2016-01-1470.
- [36] Personal communications with N. Rose on 2017-09-06.

## BIOGRAPHY



Mr. Singh is a private practice engineer with specialties in the fields of motor vehicle accident reconstruction and biomechanical engineering. He holds a BS in mechanical engineering from the University of Illinois at Urbana-Champaign and a MS in biomedical engineering from the University of Southern California. He has also authored numerous other peer reviewed conference proceedings, technical papers and scientific papers.